CrossMark

J. Fluid Mech. (2017), *vol.* 826, *pp.* 270–301. © Cambridge University Press 2017
doi:10.1017/jfm.2017.416

Biglobal instabilities of compressible open-cavity flows

Yiyang Sun[1,†], Kunihiko Taira[1], Louis N. Cattafesta III[1] and Lawrence S. Ukeiley[2]

[1]Department of Mechanical Engineering, Florida State University, Tallahassee, FL 32310, USA

[2]Department of Mechanical and Aerospace Engineering, University of Florida, Gainesville, FL 32611, USA

(Received 6 October 2016; revised 2 June 2017; accepted 11 June 2017; first published online 3 August 2017)

The stability characteristics of compressible spanwise-periodic open-cavity flows are investigated with direct numerical simulation (DNS) and biglobal stability analysis for rectangular cavities with aspect ratios of $L/D = 2$ and 6. This study examines the behaviour of instabilities with respect to stable and unstable steady states in the laminar regime for subsonic as well as transonic conditions where compressibility plays an important role. It is observed that an increase in Mach number destabilizes the flow in the subsonic regime and stabilizes the flow in the transonic regime. Biglobal stability analysis for spanwise-periodic flows over rectangular cavities with large aspect ratio is closely examined in this study due to its importance in aerodynamic applications. Moreover, biglobal stability analysis is conducted to extract two-dimensional (2-D) and 3-D eigenmodes for prescribed spanwise wavelengths λ/D about the 2-D steady state. The properties of 2-D eigenmodes agree well with those observed in the 2-D nonlinear simulations. In the analysis of 3-D eigenmodes, it is found that an increase of Mach number stabilizes dominant 3-D eigenmodes. For a short cavity with $L/D = 2$, the 3-D eigenmodes primarily stem from centrifugal instabilities. For a long cavity with $L/D = 6$, other types of eigenmodes appear whose structures extend from the aft-region to the mid-region of the cavity, in addition to the centrifugal instability mode located in the rear part of the cavity. A selected number of 3-D DNS are performed at $M_\infty = 0.6$ for cavities with $L/D = 2$ and 6. For $L/D = 2$, the properties of 3-D structures present in the 3-D nonlinear flow correspond closely to those obtained from linear stability analysis. However, for $L/D = 6$, the 3-D eigenmodes cannot be clearly observed in the 3-D DNS due to the strong nonlinearity that develops over the length of the cavity. In addition, it is noted that three-dimensionality in the flow helps alleviate violent oscillations for the long cavity. The analysis performed in this paper can provide valuable insights for designing effective flow control strategies to suppress undesirable aerodynamic and pressure fluctuations in compressible open-cavity flows.

Key words: compressible flows, instability

† Email address for correspondence: ys12d@my.fsu.edu

https://doi.org/10.1017/jfm.2017.416 Published online by Cambridge University Press

1. Introduction

Flow over an open rectangular cavity has been a fundamental research topic for decades because of its ubiquitous nature in many engineering settings, including landing gear wells, gaps between plates and aircraft weapon bays (Cattafesta *et al.* 2008; Lawson & Barakos 2011). In open-cavity flow, a shear layer emanates from the leading edge of the cavity and spans the length of the cavity. The perturbations in the shear layer are amplified through the Kelvin–Helmholtz instability, which introduce large vortical structures that impinge on the aft wall of the cavity creating intense pressure fluctuations and acoustic waves. These waves propagate upstream and induce new disturbances in the shear layer from the leading edge, which forms an acoustic feedback process that can lead to self-sustained oscillations.

The properties of these oscillations can be affected by various parameters including cavity geometry as well as the hydrodynamic and acoustic characteristics of the incoming flow (Rockwell & Naudascher 1978; Rowley, Colonius & Basu 2002; Lawson & Barakos 2011; Sun *et al.* 2014). The early work of Rossiter (1964) predicts the two-dimensional (2-D) shear-layer oscillation frequency through a semi-empirical formula based on the free stream Mach number, M_∞. Heller & Bliss (1975) later modified the formula to better match the experimental measurements. This modified formula is used as reference in the present work. The mode associated with the resonance is referred to as the Rossiter mode and its frequency f_n can be predicted in terms of the Strouhal number as

$$St_L = \frac{f_n L}{u_\infty} = \frac{n-\alpha}{1/\kappa + M_\infty/\sqrt{1+(\gamma-1)M_\infty^2/2}}, \tag{1.1}$$

where L is the length of cavity, empirical constant κ ($=0.57$) is the average convective speed of disturbance in shear layer, α ($=0.25$) (Rossiter 1964) corresponds to phase delay, γ ($=1.4$) is specific heat ratio and $n=1, 2, \ldots$ leads to the nth Rossiter mode. We also define a Strouhal number based on the cavity depth ($St_D = f_n D/u_\infty$) to quantify the frequencies of 3-D modes of open-cavity flows.

The oscillations associated with open-cavity flows are generally undesirable, because they may damage the cavity contents due to the unsteady aerodynamic forces and intense pressure fluctuations. During the past few decades, researchers have developed techniques to suppress the oscillations through various passive and active flow control strategies. A comprehensive review on active control of high Reynolds number cavity flow for a wide range of Mach numbers is given by Cattafesta *et al.* (2008). Both open- and closed-loop control techniques have demonstrated the ability to significantly reduce the pressure fluctuations and noise emission (Samimy *et al.* 2007; Cattafesta *et al.* 2008; Lusk, Cattafesta & Ukeiley 2012; Zhang *et al.* 2015). However, there has not been a clear control strategy that can be universally applied to open-cavity flows in the most general manner. As the baseline flow changes with different cavity geometry and operating conditions, the current control approaches for suppressing aerodynamic fluctuations have to be tailored for each operating condition and cavity configuration. Although flow control has been applied in some high-speed flows (Cattafesta *et al.* 2008; Cattafesta & Sheplak 2011), both effective and efficient control of transonic and supersonic cavity flows remains challenging due to a lack of actuator control authority at these flow conditions. Due to the large energy input required for high-speed cavity flows, the control authority is typically insufficient. Moreover, current actuators are characterized by a fixed gain–bandwidth product (Cattafesta & Sheplak 2011), which motivates the present study that can shed light on the proper choice of actuation parameters based on intrinsic flow instabilities.

https://doi.org/10.1017/jfm.2017.416 Published online by Cambridge University Press

	L/D	M_∞	$\beta\ (=2\pi/\lambda)$
Brès & Colonius (2008)	1, 2, 4	0.1–0.6	3.14–12.56
Yamouni, Sipp & Jacquin (2013)	1 and 2	0.0–0.9	0
Meseguer-Garrido *et al.* (2014)	1–3	0.0	0–22
de Vicente *et al.* (2014)	2	0.0	0–22
Present	2 and 6	0.1–1.4	0 and 3.14–12.56

TABLE 1. A summary of biglobal stability analysis of laminar open-cavity flows studied in past literature and the present work. Mach number 0 represents incompressible flow.

As observed in several studies on cavity flows (Maull & East 1963; Ahuja & Mendoza 1995; Arunajatesan *et al.* 2014; Beresh *et al.* 2015; Beresh, Wagner & Casper 2016; Sun *et al.* 2016*b*), three-dimensionality can affect the dominant oscillation characteristics. Although the three-dimensionality discussed in these experiments and simulations mostly relates to the significance of spanwise end effects on the flow, such end effects can modify spanwise instabilities in the flow. This suggests a potential to control cavity flow with 3-D perturbations. To understand the characteristics of the three-dimensionality in open-cavity flow, 3-D simulations can capture the unsteadiness and structures of steady saturated flow but cannot reveal the instability characteristics directly. However, with the development of numerical techniques, numerical instability analysis of cavity flows has attracted increasing attention during the last decade. In particular, linear stability analysis provides deep insights into the instability mechanisms, as well as physics-based guidelines for effective 3-D control strategies in terms of spatial and temporal parameters needed in flow control designs. Hence, in this paper, the influence of compressibility on characteristics of 2-D and 3-D global instabilities of spanwise-periodic open-cavity flows are examined thoroughly based on linear stability theory.

To analyse the 3-D instabilities of such cavity flows, we utilize biglobal stability theory to identify the properties of the 3-D instabilities associated with a given 2-D base state. The computational cost associated with this analysis is much less compared to the case in which the base state and perturbations are both considered three-dimensional. Hence, it is a widely used technique to specifically examine the spanwise instabilities of 2-D inhomogeneous flows (Theofilis 2003). In table 1, we summarize past biglobal stability analyses of open-cavity flows. Theofilis & Colonius (2004) presented the framework of the biglobal stability analysis for compressible open-cavity flows with aspect ratio $L/D = 2$ and $M_\infty = 0.325$. Following their work, several researchers reported on instability studies of open-cavity flows using linear instability analysis. Brès & Colonius (2008) characterized the onset of 2-D subsonic ($0.1 \leqslant M_\infty \leqslant 0.6$) cavity flow instabilities at low Reynolds numbers. They also performed 3-D linear simulations on compressible open-cavity flow with $L/D = 2$ and 4 and identified the spanwise wavelength of the most unstable/least stable modes via examination of the most amplified disturbances with respect to the steady base flow. They found that the 3-D modes have an order-of-magnitude lower frequency than those of the 2-D resonant modes in the cavity, with the wavelength of the most unstable mode being $\lambda/D \approx 1$. Yamouni *et al.* (2013) performed global stability analysis to investigate the interaction between the feedback aeroacoustic mechanism and acoustic resonance in the flow over a cavity with $L/D = 1$. Moreover, de Vicente *et al.* (2014) conducted global stability analysis on incompressible open-cavity flows and observed that 3-D instability modes can split into different branches

https://doi.org/10.1017/jfm.2017.416 Published online by Cambridge University Press

depending on their spanwise wavelengths. They also compared their numerical results to experiments and reported that their numerical results resembled the fully saturated nonlinear flow features seen in experiments. Considering lateral wall effects on the 3-D structures present in finite-span cavity flows, Liu, Gómez & Theofilis (2016) performed triglobal instability analysis to unravel the transition of steady laminar flow over a three-dimensional cavity for incompressible flow. All of these studies provide insights into the characteristics of spanwise instabilities associated with open-cavity flows. Nonetheless, there is still a gap in the literature with respect to instabilities of open-cavity flow in the transonic regime. Moreover, the instabilities of flows over the cavities with large $L/D = 6$, which are particularly relevant in aircraft bays, have been rarely studied. Furthermore, 3-D flow control strategies applied to realistic compressible open-cavity flows (Lusk *et al.* 2012; George *et al.* 2015; Zhang *et al.* 2015) are functions of spanwise wavelength and Mach number, for which the present work can offer insights.

One of the objectives of this paper is to perform 2-D direct numerical simulation (DNS) of flows over rectangular cavities with $L/D = 2$ and 6 to characterize the effects of free stream Mach number M_∞, Reynolds number Re_θ and aspect ratio L/D on the 2-D flow instabilities. Furthermore, the stable/unstable steady states obtained from 2-D simulations serve as base states in the biglobal stability analysis to reveal characteristics of 2-D ($\lambda/D = \infty$) and 3-D ($\lambda/D = 0.5$–2.0) eigenmodes associated with the flows. In the linear stability analysis component of this study, 2-D and 3-D global eigenmodes are identified for $M_\infty = 0.3$–1.4 and $L/D = 2$, 6. These global eigenmodes are also compared to the flow fields from the 2-D and 3-D nonlinear simulations. We will show that most of the linear stability predictions of flow properties are in a good agreement to those captured from the nonlinear flows, which could serve a foundation for parameter choice in flow control designs.

In what follows, the computational approach and numerical validation are presented in § 2. In § 3, the characteristics of the 2-D instabilities in open-cavity flows are investigated via DNS. With the stable/unstable steady states obtained from 2-D DNS, 2-D eigenmodes captured via biglobal stability analysis are discussed and compared to the flow characteristics revealed in the nonlinear simulations in § 4.1. Furthermore, 3-D eigenmodes with specified spanwise wavelengths are examined in § 4.2, in which the instabilities of 3-D modes show significant dependence on Mach number and spanwise wavelength. A comparison of the results from the DNS and biglobal stability analysis is provided in § 4.2. Finally, concluding remarks are offered in § 5.

2. Computational approach

2.1. *Direct numerical simulation set-up and validation*

Two-dimensional DNS of compressible flows over a rectangular cavity are performed using a high-fidelity compressible flow solver CharLES (Khalighi *et al.* 2011*a*,*b*; Brès *et al.* 2017) to solve the full compressible Navier–Stokes equations. A second-order finite-volume method and the third-order Runge–Kutta temporal scheme are implemented. The Harten–Lax–van Leer contact (HLLC) scheme is used to capture the shocks formed in supersonic flow (Toro 2009). The variables including the spatial coordinate x_i, time t, density ρ, velocity u_i, energy e, pressure P, temperature T, are non-dimensionalized as

$$x_i = \frac{x_i^d}{D^d}, \quad t = \frac{t^d a_\infty^d}{D^d}, \quad \rho = \frac{\rho^d}{\rho_\infty^d}, \quad u_i = \frac{u_i^d}{a_\infty^d}, \quad e = \frac{e^d}{\rho_\infty^d (a_\infty^d)^2}, \quad P = \frac{P^d}{\gamma P_\infty^d}, \quad T = \frac{T^d}{T_\infty^d}, \tag{2.1a–g}$$

https://doi.org/10.1017/jfm.2017.416 Published online by Cambridge University Press

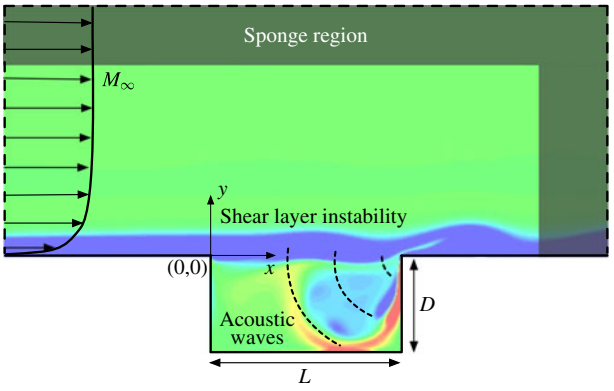


FIGURE 1. (Colour online) Computational set-up for open-cavity flow (not to scale).

where variables with superscript d refer to the dimensional quantities and those with the subscript ∞ denote the free stream values. The x-, y- and z-directions represent the streamwise, wall-normal and spanwise directions, respectively. A structured mesh with non-uniform spacing in both x- and y-directions is used for the simulations. Cavity flows are specified by L/D, where L and D represent the length and depth of the cavity, respectively, initial boundary layer momentum thickness θ_0 at the leading edge of the cavity and free stream Mach number $M_\infty \equiv u^d_\infty / a^d_\infty$. The free stream sonic speed is denoted by a^d_∞. The Reynolds number based on the initial momentum boundary layer thickness θ_0 and the Prandtl number are respectively defined as

$$Re_\theta \equiv \frac{\rho_\infty u_\infty \theta_0}{\mu_\infty} \quad \text{and} \quad Pr \equiv \frac{c_p \mu_\infty}{k}, \tag{2.2a,b}$$

where μ_∞ is the dynamic viscosity, c_p is the specific heat and k is the thermal conductivity.

In the present investigation, we consider two-dimensional cavities with $L/D = 2$ and 6. The former geometry serves as the basis for comparison with those reported in the literature, while the latter is representative of a prototypical cavity application on aircraft. As illustrated in figure 1, the origin is placed at the leading edge of the cavity. The initial momentum boundary layer thickness θ_0 is prescribed at the leading edge, and the distance between the upstream wall boundary and the leading edge is adjusted accordingly for the chosen Re_θ. The outflow boundary is placed $7D$ from the trailing edge of the cavity. The normal distance from the cavity surface to the top boundary of the computational domain is maintained at $9D$. The size of computational domain follows the work of Colonius, Basu & Rowley (1999), in which they studied the effects of the computational domain on the flows and identified the appropriate size of the domain. No-slip and adiabatic boundary conditions are specified at the upstream and downstream floors as well as the walls of the cavity. To damp out exiting acoustic waves and wake structures, sponge zones (Freund 1997) are applied to the outlet and top boundaries spanning a length of $2D$ from computational boundaries. The computational domain for three-dimensional DNS extends the two-dimensional set-up with spanwise periodicity for a width-to-depth ratio of $W/D = 2$ (which is suitable for $\lambda/D \leqslant 2$) with 64 grid points spaced uniformly in the spanwise direction.

The effect of Mach number is analysed from the subsonic regime to the transonic regime with Reynolds number Re_θ from 5 to 144 for flows over cavities with $L/D = 2$

https://doi.org/10.1017/jfm.2017.416 Published online by Cambridge University Press

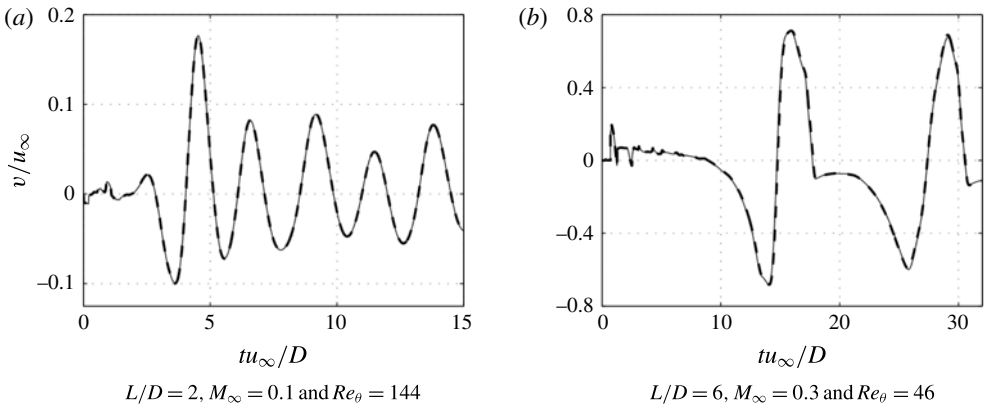


FIGURE 2. Comparison of the v-velocity at the midpoint ($x = L/2$, $y = 0$) of the cavity. The solid line shows the baseline case with half a million grid points and the dashed line represents the refined case with 1.1 million grid points.

	St_{L1}	St_{L2}
Rossiter (1964)	0.321	0.750
Brès (2007)	0.404	0.698
Present	0.412	0.715

TABLE 2. Comparison of Rossiter modes I and II frequencies for open-cavity flow with $L/D = 2$, $Re_\theta = 56.8$ and $M_\infty = 0.6$.

and 6. To initialize the flow field, an incompressible Blasius boundary layer profile is imposed over the entire computational domain above the floor, while the flow inside the cavity is set to be quiescent. Consistent with the chosen Reynolds number range of this study, the incompressible Blasius boundary layer profile is utilized as the variation in boundary layer thickness for the range of Mach numbers from 0 to 1.4 is less than 10 % (White 1991). As the Blasius profile is characterized by the momentum boundary layer thickness, we fix the ratio of the cavity depth to the initial momentum thickness $D/\theta_0 = 26.4$ for all the cases considered in the present study.

A grid convergence study for both rectangular cavity geometries ($L/D = 2$ and 6) is performed. Presented in figure 2 are two grid convergence comparisons performed with $Re_\theta = 144$ and $M_\infty = 0.1$ for $L/D = 2$ and $Re_\theta = 46$ and $M_\infty = 0.3$ for $L/D = 6$. The baseline computation is conducted on a structured mesh with approximately half a million grid points. A finer mesh with one million grid points is also performed for comparison. The v-velocity history at the midpoint location ($x = L/2$, $y = 0$) over the cavity is shown in figure 2. The baseline mesh of half a million grid points is shown to be sufficient to achieve numerical convergence. Moreover, the frequencies of the oscillations in the flow for $L/D = 2$, $Re_\theta = 56.8$ and $M_\infty = 0.6$ are compared to the prediction from Rossiter's semi-empirical formula and the work by Brès (2007) in table 2, exhibiting good agreement.

Furthermore, instantaneous density gradient flow fields at $M_\infty = 0.8$ and 1.4 are compared to the experimental schlieren images by Krishnamurty (1956) and numerical results by Rowley *et al.* (2002) in figure 3. In the experiments conducted by Krishnamurty (1956), the cavity width is almost 40 times the depth ($W/D \approx 40$).

https://doi.org/10.1017/jfm.2017.416 Published online by Cambridge University Press

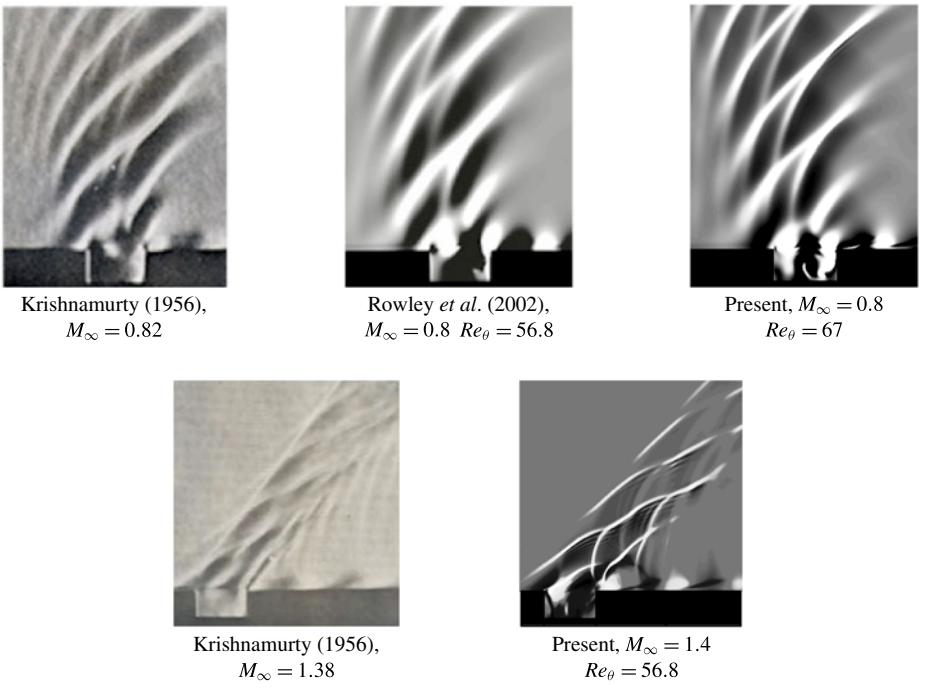


FIGURE 3. Comparison of schlieren images by Krishnamurty (1956), DNS by Rowley *et al.* (2002) (reproduced with permission from Cambridge University Press) and the present work ($\partial\rho/\partial x$) at $M_\infty = 0.8$ and 1.4.

Hence, the results from this experimental study can be regarded as approximately two-dimensional. As shown in figure 3, the present results exhibit good agreement with the experiments and previous simulation results. For $M_\infty = 0.8$, the acoustic waves generated at the trailing edge of cavity propagate upstream, and for the $M_\infty = 1.4$ case, the acoustic wave structures are aligned in an oblique manner. Further analysis of the open-cavity flow features are provided in § 3.

2.2. *Biglobal stability analysis set-up and validation*

Biglobal stability analysis is performed with respect to the base flow obtained from the 2-D nonlinear simulation to uncover the compressible spanwise-periodic global instabilities. The state vector $\boldsymbol{q} = [\rho, \rho u, \rho v, \rho w, e]^{\mathrm{T}}$ is decomposed into base state $\bar{\boldsymbol{q}}(x, y)$ and perturbations $\boldsymbol{q}'(x, y, z, t)$ as

$$\boldsymbol{q}(x, y, z, t) = \bar{\boldsymbol{q}}(x, y) + \boldsymbol{q}'(x, y, z, t). \tag{2.3}$$

The steady solution (base state) $\bar{\boldsymbol{q}}$ satisfies the Navier–Stokes equations and $\boldsymbol{q}'$ is small in its magnitude compared to the base state ($|\boldsymbol{q}'| \ll |\bar{\boldsymbol{q}}|$). In the present work, the base state $\bar{\boldsymbol{q}}$, obtained from the 2-D DNS, is either a time-invariant stable state or an unstable steady state calculated by the selective frequency damping method (Åkervik *et al.* 2006). By substituting (2.3) into the Navier–Stokes equations and the equation of state, the governing equations are linearized by retaining only the linear terms of

https://doi.org/10.1017/jfm.2017.416 Published online by Cambridge University Press

$\boldsymbol{q}'$ which yields the following set of linear equations for $\boldsymbol{q}'$

$$\left.\begin{aligned}
&\frac{\partial \rho'}{\partial t}+\frac{\partial}{\partial x_j}(\rho'\bar{u}_j+\bar{\rho}u_j')=0,\\
&\frac{\partial}{\partial t}(\rho'\bar{u}_i+\bar{\rho}u_i')+\frac{\partial}{\partial x_j}(\bar{\rho}\bar{u}_iu_j'+\bar{\rho}u_i'\bar{u}_j+\rho'\bar{u}_i\bar{u}_j+P'\delta_{ij})\\
&\quad=\frac{1}{Re}\frac{\partial}{\partial x_j}\left(\frac{\partial u_i'}{\partial x_j}+\frac{\partial u_j'}{\partial x_i}-\frac{2}{3}\frac{\partial u_k'}{\partial x_k}\delta_{ij}\right),\\
&\frac{\partial e'}{\partial t}+\frac{\partial}{\partial x_j}\left[(\bar{e}+\bar{P})u_j'+(e'+P')\bar{u}_j\right]\\
&\quad=\frac{1}{Re}\frac{\partial}{\partial x_j}\left[\bar{u}_i\left(\frac{\partial u_i'}{\partial x_j}+\frac{\partial u_j'}{\partial x_i}-\frac{2}{3}\frac{\partial u_k'}{\partial x_k}\delta_{ij}\right)+u_i'\left(\frac{\partial \bar{u}_i}{\partial x_j}+\frac{\partial \bar{u}_j}{\partial x_i}-\frac{2}{3}\frac{\partial \bar{u}_k}{\partial x_k}\delta_{ij}\right)\right]\\
&\qquad+\frac{1}{Re}\frac{1}{Pr}\frac{\partial^2 T'}{\partial x_k\partial x_k}
\end{aligned}\right\}\tag{2.4}$$

along with the linearized equation of state

$$P'=R(\rho'\bar{T}+\bar{\rho}T'),\tag{2.5}$$

where R is the gas constant.

The above linear governing equations permit modal perturbations of the form

$$\boldsymbol{q}'(x,y,z,t)=\hat{\boldsymbol{q}}(x,y)\mathrm{e}^{\mathrm{i}(\beta z-\omega t)}+\text{complex conjugate}.\tag{2.6}$$

Upon substitution of this modal expression into the linearized Navier–Stokes equations (2.4), we can transform the instability analysis from solving an initial value problem to an eigenvalue problem of

$$\mathcal{A}(\bar{\boldsymbol{q}};\beta)\hat{\boldsymbol{q}}=\omega\hat{\boldsymbol{q}}.\tag{2.7}$$

Temporal instability is examined by inserting a real wavenumber β with its corresponding wavelength $\lambda/D=2\pi/\beta$. The corresponding eigenmodes consist of eigenvectors $\hat{\boldsymbol{q}}(x,y)=\hat{\boldsymbol{q}}_r(x,y)+\mathrm{i}\hat{\boldsymbol{q}}_i(x,y)$ and their complex eigenvalues $\omega=\omega_r+\mathrm{i}\omega_i$, where $\hat{\boldsymbol{q}}_r$ and $\hat{\boldsymbol{q}}_i$ represent real and imaginary components of eigenvectors; ω_r and ω_i are the modal frequency and growth ($\omega_i>0$) or decay ($\omega_i<0$) rate, respectively. While solving for the eigenmodes, the linear operator $\mathcal{A}\in\mathbb{C}^{5n\times 5n}$ and eigenvector $\hat{\boldsymbol{q}}\in\mathbb{C}^{5n}$ for $n=O(10^6)$ grid points, can become extremely large. For this large-scale eigenvalue problem, the ARPACK library (Sorensen *et al.* 1996–2008), with an implicitly restarted Arnoldi method, is used in the current study to solve for the eigenmodes. The present approach is based on a matrix-free computation. Since the linear governing equations for the perturbation variables are explicit in their forms, we use the regular mode (not shift-and-invert transformation) in ARPACK and only provide the matrix vector products $A(\bar{q};\beta)\hat{q}$ repeatedly to the solver, which avoids requesting large memory space to store matrix entries while solving the eigenvalue problem. All the eigenmodes reported in this paper are converged with $\|\omega\hat{q}-A\hat{q}\|\leqslant O(10^{-10})$. Along the cavity walls, velocity perturbations and the wall-normal gradient of pressure perturbation are set to zero. According to the governing equations, the boundary condition for density perturbation is not required because the momentum perturbation flux is zero due to zero velocity along the wall. For the inlet, density and velocity perturbations, as well as the pressure gradient, are

https://doi.org/10.1017/jfm.2017.416 Published online by Cambridge University Press

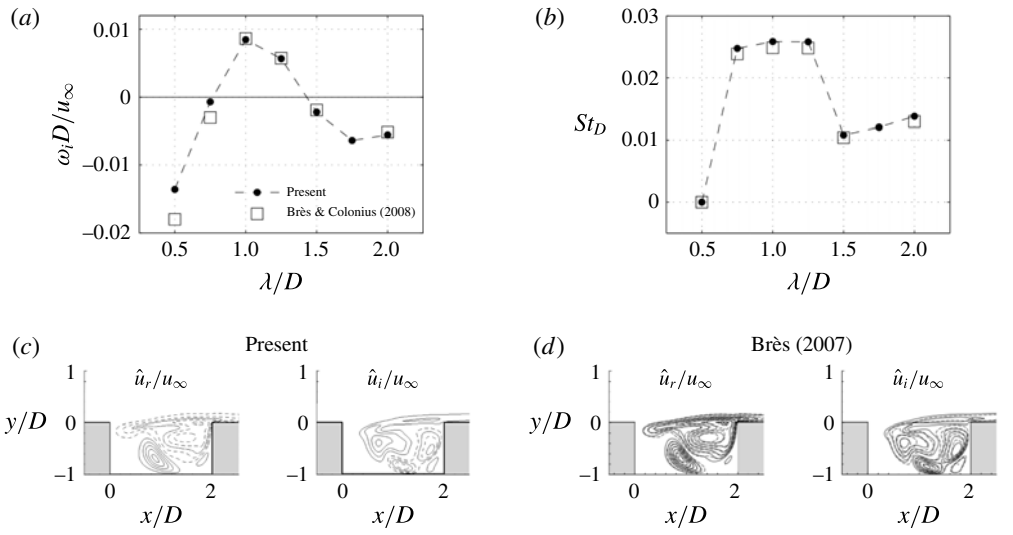


FIGURE 4. Comparison of dominant 3-D modes properties ((*a*) growth/decay rate $\omega_i D/u_\infty$ and (*b*) frequency St_D) between the present biglobal analysis and linear simulation by Brès & Colonius (2008) at $Re_\theta = 56.8$. Eigenvectors of the most unstable mode with $\lambda/D = 1.0$ are in good agreement with those in Brès (2007), contour levels of real and imaginary components of streamwise velocity $\hat{u}_r/u_\infty$ and $\hat{u}_i/u_\infty \in [-0.058, 0.058]$ are used. (*c*) Present: $M_\infty = 0.3$; (*d*) Brès (2007): $M_\infty = 0.325$ (reproduced with permission from the author).

prescribed to be zero. For the outflow and far field boundaries, gradients of density, velocity and pressure are prescribed as zero. Moreover, an adiabatic condition is assumed for all boundaries. The base state is interpolated on a coarse mesh for the eigenvalue problem (Bergamo *et al.* 2015). An investigation of domain size was conducted to assure the convergence of eigenspectrum. A grid resolution study was performed to ensure accurate stability results. Additional details on the computational procedures can be found in Sun *et al.* (2016*a*).

The validation of global instability analysis is performed on the flow at $M_\infty = 0.3$ and $Re_\theta = 56.8$ with $L/D = 2$. As shown in figure 4, the dominant 3-D modes from this study are compared to the results from Brès & Colonius (2008), in which they resolved the dominant 3-D modes by solving an initial value problem based on the linearized Navier–Stokes equations. The growth/decay rate, frequency and eigenvector of the dominant eigenmode obtained from present instability study agree well with those from Brès & Colonius (2008).

3. Two-dimensional direct numerical simulation and analysis

We focus on examining the effects of L/D, Mach number, and Reynolds number on 2-D flow oscillation mechanisms in this section. These parameters are known to significantly influence cavity flows (Krishnamurty 1956; Rowley *et al.* 2002; Brès & Colonius 2008; Lawson & Barakos 2011). In general, flows over open cavities have been broadly classified into stable, shear-layer and wake-mode dominated flows. For a stable case, the flow reaches a time-invariant steady state. With the shear-layer (Rossiter) mode, disturbances convecting downstream are amplified in the shear layer.

https://doi.org/10.1017/jfm.2017.416 Published online by Cambridge University Press

The wake mode is rarely observed in experiments but is captured in simulations at low Reynolds number when the cavity length is relatively large compared to the momentum boundary layer thickness at the leading edge (Rowley *et al.* 2002; Sun *et al.* 2016*a*). It was also observed by Gharib & Roshko (1987) and Zhang & Naguib (2011) for incompressible axisymmetric cavity flow in their experiments. The primary feature of the wake mode is the shedding of large vortices leading to the interaction between the vortex and the trailing edge, causing violent fluctuations in the cavity.

Here, we discuss the flow characteristics, instabilities, and behaviour of the Rossiter mode by performing 2-D DNS. The simulations were conducted over a sufficiently long convective time (with a minimum of 150 convective units D/u_∞) for the flow to reach a steady state. Such flow in this study is categorized as stable (asymptotically stable) if the flow is devoid of any oscillation and otherwise unstable. A number of cases that span the range of Mach numbers from $M_\infty = 0.1$ to 1.4 and Reynolds number (Re_θ) up to 144 with $L/D = 2$ and 6 are analysed in detail. For $L/D = 2$, the parameters of M_∞ and Re_θ are chosen to greatly expand upon the subsonic stability analysis performed by Brès & Colonius (2008). We extend their analysis to the transonic Mach number regime and determine unstable steady states of oscillatory cavity flows in preparation for the biglobal stability analysis in § 4. Flow over a long cavity with $L/D = 6$ is also examined in detail as this configuration is representative of long cavities used in aircraft.

3.1. *Flow field characteristics*

To examine how compressibility affects flow features, the instantaneous density gradient field, the instantaneous vorticity field and the time-averaged streamlines are shown in figures 5 and 6 for cavities with $L/D = 2$ and 6, respectively.

For a cavity with $L/D = 2$, the instantaneous density gradient fields for Mach numbers from 0.6 to 1.4 are presented in figure 5 at $Re_\theta = 46$. At $M_\infty = 0.6$, the compression waves in the flow field are not prominent compared to those at higher Mach numbers. When M_∞ increases to 0.8, the acoustic radiation emitted from the trailing edge becomes noticeable and its wavelength becomes smaller, which has also been discussed by Rowley *et al.* (2002). For $M_\infty \geqslant 1.0$, the acoustic waves are more prominent and its structure over the cavity becomes directional. This phenomenon is observed in experiments by Krishnamurty (1956) as well. Part of the compression waves are generated at the rear corner of cavity. At the trailing edge, for the oncoming flow with a large deflection angle, a shock is formed due to the impingement of the shear layer on the trailing edge. The remaining waves are generated from the periodic expansion and compression of shear-layer oscillations in the supersonic flow. Inside the cavity, animations (not shown) reveal that waves travel back and forth due to reflections. Outside of the cavity, compression waves propagate upstream in the subsonic cases ($M_\infty < 1.0$). On the other hand, the compression waves are swept downstream in the supersonic cases ($M_\infty \geqslant 1.0$). This leads to the formation of oblique compression waves propagating downstream. A beam structure is formed which consists of the compression waves described above. The angle φ of the beam composed of these compression waves above the cavity is measured in the density gradient flow fields. This angle φ approximates the corresponding Mach wave angle $\sin^{-1}(1/M_\infty)$ for $M_\infty > 1$. For $M_\infty = 1.2$ and 1.4, we find $\varphi = 60.0^\circ$ and 46.0° with $\sin^{-1}(1/M_\infty) = 56.4^\circ$ and 45.6°, respectively.

As shown in figure 6, for a cavity with $L/D = 6$ at $Re_\theta = 19$, large density gradients are caused by expansion and compression of the shear layer for the subsonic regime

https://doi.org/10.1017/jfm.2017.416 Published online by Cambridge University Press

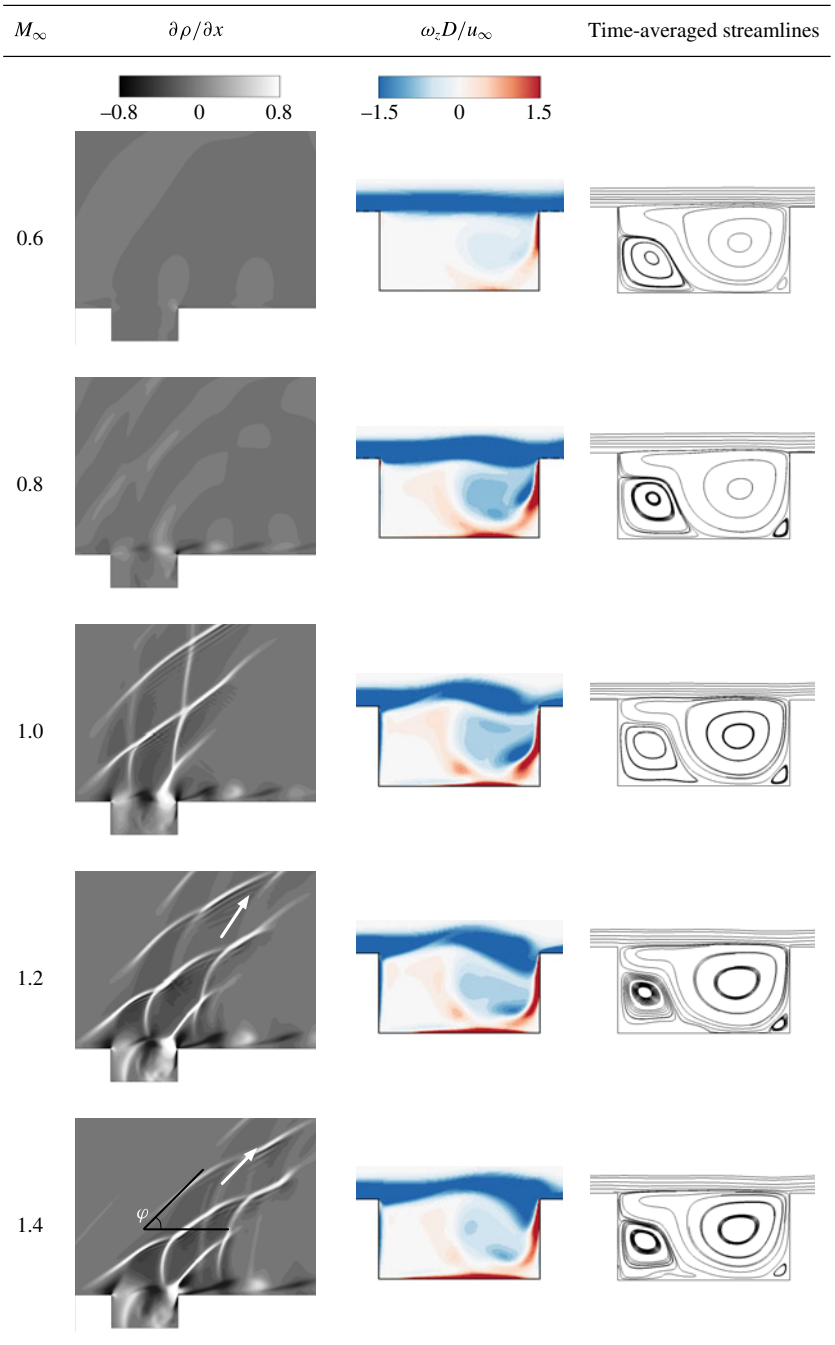


FIGURE 5. (Colour online) Instantaneous numerical schlieren $\partial\rho/\partial x \in [-0.8, 0.8]$, instantaneous vorticity $\omega_z D/u_\infty \in [-1.5, 1.5]$ contours and time-averaged streamlines are shown for $M_\infty = 0.6$–1.4, $L/D = 2$ and $Re_\theta = 46$. The arrows in numerical schlieren images indicate the propagation directions of compression waves.

https://doi.org/10.1017/jfm.2017.416 Published online by Cambridge University Press

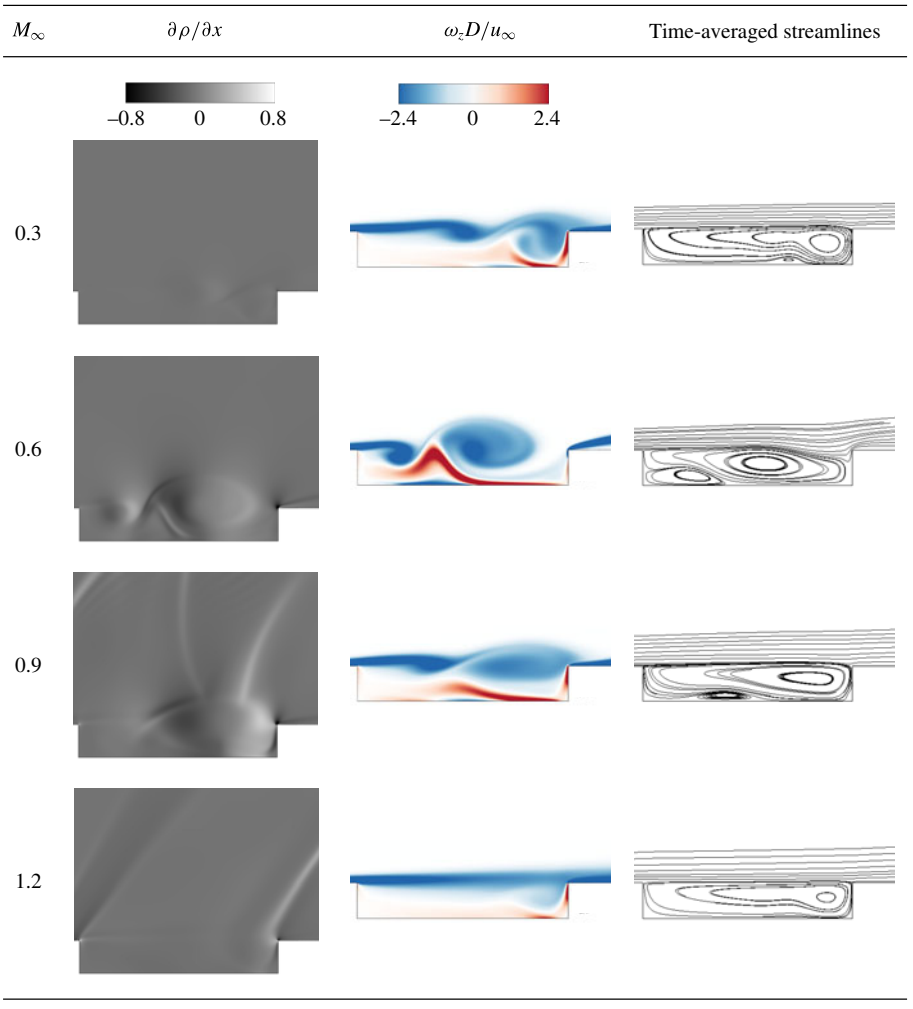


FIGURE 6. (Colour online) Instantaneous numerical schlieren $\partial\rho/\partial x \in [-0.8, 0.8]$, instantaneous vorticity $\omega_z D/u_\infty \in [-2.4, 2.4]$ contours and time-averaged streamlines are shown for $M_\infty = 0.3$–1.2, $L/D = 6$ and $Re_\theta = 19$.

($M_\infty = 0.3$ and 0.6). However, for $M_\infty = 0.9$, the acoustic waves become observable with their wavelength corresponding to the length of the cavity. At $M_\infty = 1.2$, the flow becomes stable with weak Mach waves emanating from the leading and trailing edges.

For a cavity with L/D = 2, we only observe the shear-layer mode for unstable flows, with a large clockwise-rotating vortex present in the rear part of the cavity as shown in figure 5. In all cases considered for the short cavity, the streamlines reveal two major recirculation zones inside the cavity. The lack of variation in the time-averaged streamlines versus Mach number suggests that compressibility does not affect the mean flow inside the cavity significantly.

However, the flow features in the $L/D = 6$ cases vary greatly with Mach number. At $M_\infty = 0.3$, instantaneous vorticity flow fields shown in figure 6, reveal a shear-layer mode with a clockwise rotating vortex sitting near the trailing edge. An increase in M_∞ from 0.3 to 0.6 causes the flow oscillate more violently with a transition from

https://doi.org/10.1017/jfm.2017.416 Published online by Cambridge University Press

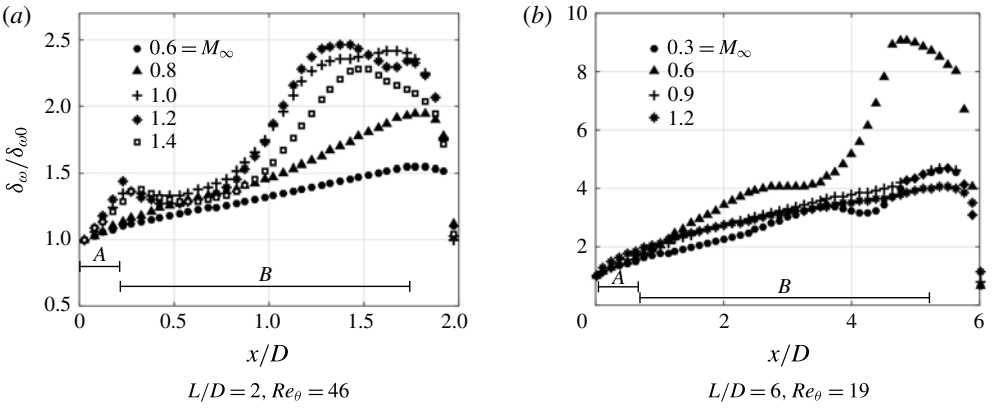


FIGURE 7. Vorticity thickness normalized by its value $\delta_{\omega 0}$ at the leading edge is shown as a function of streamwise location. Different regions are indicated by A ($x/L \in [0, 0.12]$) and B ($x/L \in [0.12, 0.86]$).

the shear-layer mode to the wake mode. The wake mode (at $M_\infty = 0.6$) dominates the flow with a large-scale vortex rolling up with an opposite sign vortex sheet being engulfed between the vortices. Details on the appearance of the wake mode are reported in Sun *et al.* (2016*a*). For $M_\infty = 0.9$, the opposite sign vorticity patch pulled between the shedding vortices decreases, and the fluctuations over the cavity weaken. In the transonic regime, increasing the Mach number from 0.9 to 1.2 leads to a steady flow. Compressibility apparently affects the flow instabilities by first destabilizing at subsonic speeds and then eventually stabilizing at transonic speeds.

A large difference between flow states versus Mach number is revealed in the time-averaged streamlines. When the free stream Mach number increases from 0.3 to 0.6, the centre of the main recirculation region moves towards the leading edge, then moves back towards to the trailing edge for $M_\infty = 0.9$. The features of flows inside the longer cavity are somewhat more complex than those of the shorter length.

The complexity of open-cavity flow results from the feedback process associated with the shear-layer development. Let us further investigate the characteristics of the shear layer over the cavity. Several researchers have noted the similarities between the shear layer spanning the cavity and a free shear layer, such as their linear spreading rate (Sarohia 1975; Cattafesta *et al.* 1997; Rowley *et al.* 2002). We evaluate the development of the vorticity thickness

$$\delta_\omega = M_\infty \left[\left(\frac{\partial \bar{u}}{\partial y} \right)_{max} \right]^{-1}. \tag{3.1}$$

In figure 7, the vorticity thickness is normalized by its value at the leading edge $\delta_{\omega 0}$. We examine the spreading rate dependence on different regions in the shear layer and only report $\mathrm{d}\delta_\omega/\mathrm{d}x$ for the cases with linear spreading rate, which are summarized in table 3.

As shown in figure 7 for the cavity with $L/D = 2$, for the cases ($M_\infty = 0.6$ and 0.8) without intense acoustic compression waves, the overall spreading rate is still nearly linear. Rowley *et al.* (2002) found $\mathrm{d}\delta_\omega/\mathrm{d}x = 0.05$ for $D/\theta_0 = 26.5$ at $Re_\theta = 56.8$ and $M_\infty = 0.6$, and the value is close to the spreading rate $\mathrm{d}\delta_\omega/\mathrm{d}x = 0.062$ (region B) for $D/\theta_0 = 26.4$ at a lower $Re_\theta = 46$ and $M_\infty = 0.6$ in the present work. In the cases with

https://doi.org/10.1017/jfm.2017.416 Published online by Cambridge University Press

$L/D=2$			$L/D=6$		
M_∞	A	B	M_∞	A	B
0.6	0.105	0.062	0.3	0.134	0.097
0.8	0.118	0.094	0.6	0.180	—
1.0	0.341	—	0.9	0.186	0.104
1.2	0.446	—	1.2	0.170	0.061
1.4	0.237	—			

TABLE 3. Spreading rate of vorticity thickness $\mathrm{d}\delta_\omega/\mathrm{d}x$ of flows over $L/D=2$ cavity for $M_\infty=0.6$ to 1.4 at $Re_\theta=46$ and $L/D=6$ cavity for $M_\infty=0.3$ to 1.2 at $Re_\theta=19$ as illustrated in figure 7. Different regions are indicated by A ($x/L\in[0, 0.12]$) and B ($x/L\in[0.12, 0.86]$).

$M_\infty\geqslant 1.0$, a double-hump distribution of vorticity thickness is observed in figure 7(*a*). As the numerical schlieren reveals in figure 5, strong compression waves are formed in supersonic flows. When these waves propagate upstream, they interact with shear layer over the cavity, which distorts the mean profile of the shear layer and results in the double-hump feature. However, for subsonic flows, the compression waves are not strong enough to affect the mean profile, resulting in a linear spreading rate. Near the leading edge of cavity (region A), the spreading rate is increased as Mach number increases until $M_\infty=1.2$. Further increasing Mach number to $M_\infty=1.4$ reduces the spreading rate. The stabilizing effect of compressibility in the transonic regime will be further addressed in a later discussion in § 4.1.

For $L/D=6$, except for the wake-mode case at $M_\infty=0.6$, all the other cases (shear-layer modes) reveal approximately linear spreading rates. We note that the growth rates here (region B) are in agreement with the values reported by Gharib & Roshko (1987), which are almost constant $\mathrm{d}\delta_\omega/\mathrm{d}x=0.124$ when $L/\theta_0>103$. The flow at $M_\infty=1.2$ is stable, in which there is no roll up of the shear layer bridging the cavity; thus the spreading rate in region B is reduced compared to the other shear-layer cases.

3.2. *Stability diagram*

In the present work, the parameters of M_∞ and Re_θ are selected to expand upon the subsonic stability analysis performed by Brès & Colonius (2008). Through an extensive parametric study, the influence of M_∞ and Re_θ on the stability of 2-D open-cavity flows are revealed, as shown in figure 8. We find the approximate neutral stability curve via nonlinear flow simulations to separate the stable and unstable zones in terms of M_∞ and Re_θ. For both $L/D=2$ and 6, when the Mach number decreases towards the incompressible limit, the flow becomes more stable for a wider range of Reynolds numbers as shown in figure 8. In the subsonic regime below $M_\infty=0.6$, an increase in Mach number destabilizes the flow, which was also documented by Brès & Colonius (2008). However, in the present study, as the Mach number increases above $M_\infty=0.6$ for both $L/D=2$ and 6, the slope of the neutral stability curve increases, which corresponds in the simulations to a reduction in the amplitude of the observed oscillations. This destabilization ($M_\infty\leqslant 0.6$) and subsequent stabilization ($M_\infty>0.6$) effects of Mach number are also reported by Yamouni *et al.* (2013) for short cavities with $L/D=1$ and 2. Compared to $L/D=2$, the neutral stability curve for $L/D=6$ shifts downwards. The flows over cavities with larger aspect ratio are thus more unstable because of the increased spatial extent for the shear layer to develop and amplify disturbances.

https://doi.org/10.1017/jfm.2017.416 Published online by Cambridge University Press

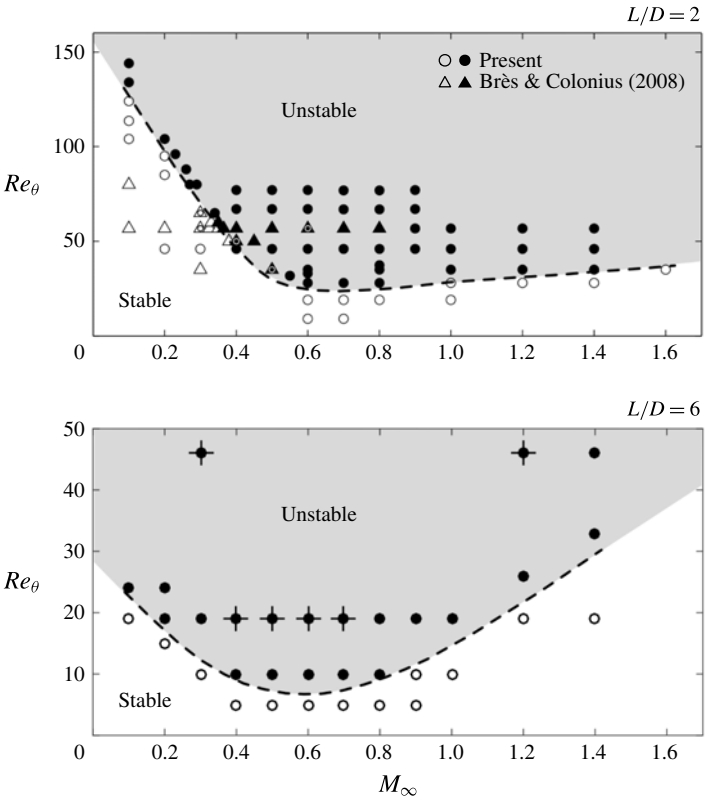


FIGURE 8. Stability diagram of 2-D open-cavity flow for $L/D = 2$ and 6 obtained from DNS. Stable cases: △, ○; unstable cases: ▲, ●. The triangles are from Brès & Colonius (2008) and the circles are from the present study. The dashed lines represent the approximate neutral stability curves. For the cavity with $L/D = 6$, the wake-mode dominated cases are indicated by $+$.

3.3. *Rossiter modes*

The primary oscillation mechanism in open-cavity flow is associated with the Rossiter modes. For all cases considered herein, the time history of the vertical velocity at the mid-point of the cavity shear layer ($x = L/2,\ y = 0$) is recorded. A discrete Fourier transform is performed on the probe data collected after a minimum of 50 convective units to eliminate the initial transients. For the unstable cases, the extracted oscillation frequencies are compared with Rossiter's prediction based on the modified formula (Heller & Bliss 1975), equation (1.1). The dominant and subdominant Rossiter modes as a function of Mach number are presented in figure 9. The frequencies (Strouhal numbers) of the Rossiter modes show a decreasing trend with increasing M_∞, which follows the prediction of the semi-empirical formula.

From the previous work by Brès (2007) on $L/D = 2$, it was inferred that Rossiter mode I dominates the flow oscillation in the subsonic regime ($0.3 \leqslant M_\infty \leqslant 0.6$). The present investigation reveals that the dominant Rossiter mode shifts to mode II with an increase in Mach number. This transition indicated by the shaded grey line in figure 9 occurs at progressively lower Mach numbers for higher Reynolds numbers. The dominant mode switching was also observed in the experimental results from

https://doi.org/10.1017/jfm.2017.416 Published online by Cambridge University Press

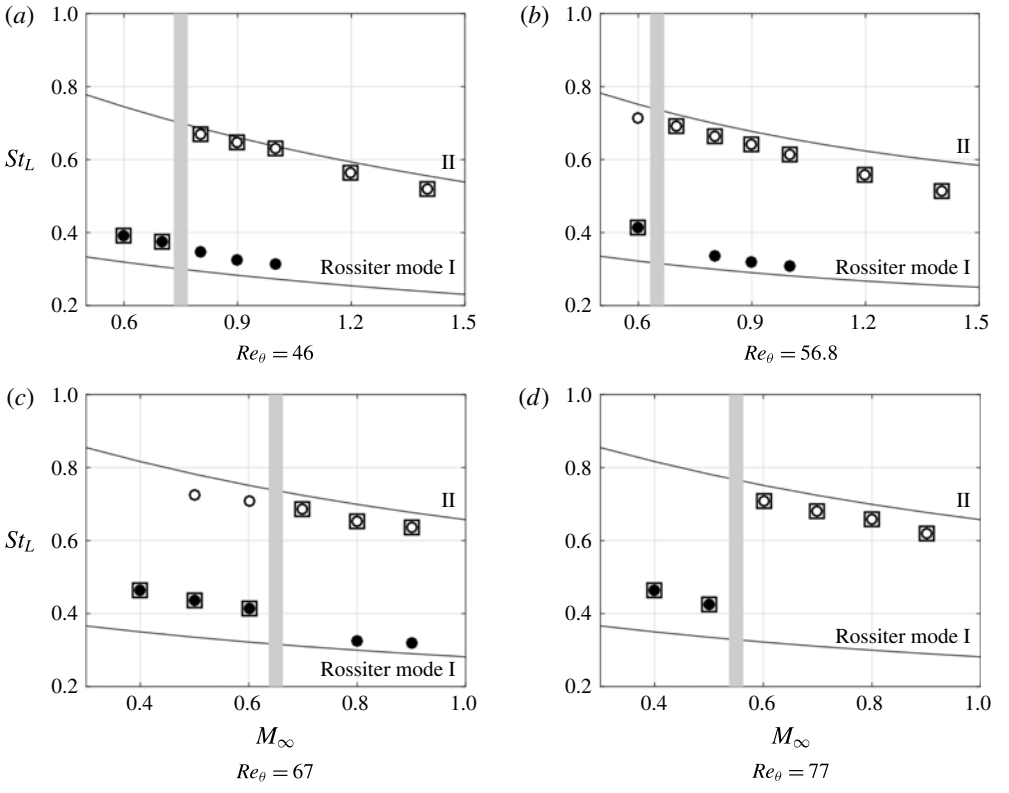


FIGURE 9. Comparison of $St_L(= St_D \cdot L/D)$ from the classic Rossiter semi-empirical formula, equation (1.1) (solid line) and the present work for $L/D = 2$. Rossiter mode I: •; mode II: ○. The dominant modes are indicated by □. The shaded grey line shows the estimate of the Mach number where the dominant mode shifts.

Kegerise *et al.* (2004) for cavity with $L/D = 2$ at a much higher Reynolds number. As shown above in figure 5 at $Re_\theta = 46$, the acoustic radiation becomes stronger at $M_\infty = 0.8$, where the dominant Rossiter mode shifts from mode I to II. Thus, it appears that the strong acoustic wave emission can be correlated with Rossiter mode II rather than mode I for the short cavity.

For flow over a cavity with $L/D = 6$, the frequencies (Strouhal numbers) of Rossiter mode for $Re_\theta = 10$ and 19 are shown in figure 10. At $Re_\theta = 10$, Rossiter mode II is the dominant mode and it is the sole mode present. As Re_θ increases to 19, the flow is unstable for $M_\infty = 0.2$ and 0.3. Moreover, the wake mode appears in the flows for a range of $M_\infty \in [0.4, 0.7]$, in which the dominant wake-mode frequency and its harmonics are observed. Although the wake-mode frequencies are close to the value of Rossiter mode frequencies, the features of the flow fields are significantly different from the shear-layer modes. Relating back to the stability diagram in figure 8 of $L/D = 6$ at $Re_\theta = 19$, we also find that the flow exhibits a shear-layer mode near the neutral stability boundary. For longer cavity flows with $L/D = 6$, there is no dominant Rossiter mode shifting observed in the shear-layer mode cases; and the wake mode dominates the flow at $M_\infty \in [0.4, 0.7]$.

The analysis performed above reveals the 2-D open-cavity flow physics and the tendency of the flow towards specific Rossiter modes. Noting that the results from

https://doi.org/10.1017/jfm.2017.416 Published online by Cambridge University Press

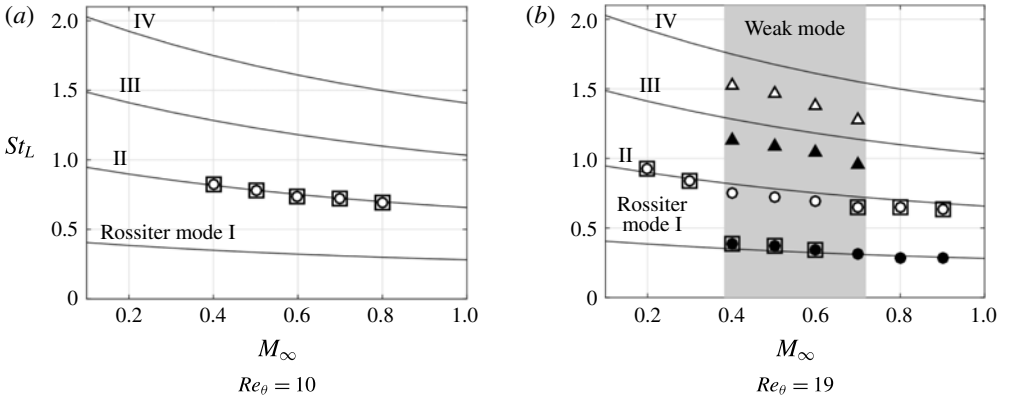


FIGURE 10. Comparison of $St_L(= St_D \cdot L/D)$ from the classic Rossiter semi-empirical formula, equation (1.1) (solid line) and present work for $L/D = 6$. The wake-mode dominated cases are indicated in the shaded region with $M_\infty \in [0.4, 0.7]$, while other cases represent shear-layer modes. In the wake-mode dominated flow, symbols •, ○, ▲ and △ represent wake mode and its harmonics. In the shear-layer mode, these symbols denote Rossiter mode I to IV. The dominant modes are indicated by □.

this section are obtained from 2-D numerical simulations. In § 4, biglobal stability analysis is employed to gain deeper insights into the flow instabilities for a range of spanwise wavenumbers, β. Two-dimensional global stability can be uncovered with $\beta = 0$, while spanwise-periodic 3-D global eigenmodes can be revealed by specifying $\beta > 0$. Because 2-D base states are required for performing the biglobal stability analysis, the results from the above nonlinear simulations serve as the foundation for the subsequent stability analysis, in addition to the unstable steady states discussed below.

3.4. *Unstable steady states*

A steady-state flow is a time-invariant solution of the Navier–Stokes equations, which can be used as base state in linear stability analysis. This base state might be stable or unstable depending on the flow conditions. Time-averaged flow is obviously time invariant but is not necessarily a solution of the Navier–Stokes equation. Numerical techniques can be used to determine the unstable steady state even if the flow is naturally unstable.

In the present work, the selective frequency damping method (Åkervik *et al.* 2006) is used to find the unstable steady state for unstable flows with the feedback gain chosen to be $\chi = 0.1$. It has been verified that the numerically found time-invariant solutions from the selective frequency damping method are indeed the unstable steady states by substituting them into the Navier–Stokes equations and ensuring that $|\dot{q}| < 10^{-7}$. As shown in figure 11, we find that the unstable steady states remain similar regardless of the Mach number variation in the short cavity ($L/D = 2$), exhibiting the same features of the time-averaged streamlines as shown in figure 5. For the cavity with $L/D = 6$, all the stable and unstable steady states share similar features regardless of the Mach number, while the time-averaged flow fields vary significantly depending on the Mach number as shown in figure 6. In the present paper, we use these steady states (in figure 11) as the base states to perform global stability analysis.

https://doi.org/10.1017/jfm.2017.416 Published online by Cambridge University Press

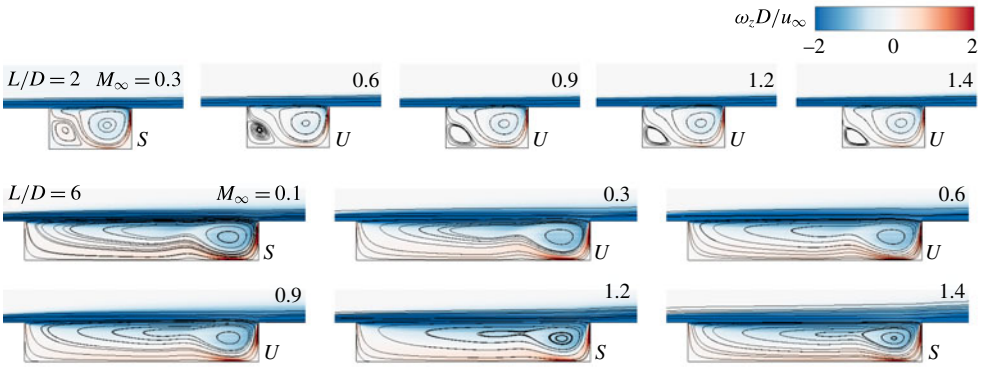


FIGURE 11. (Colour online) Streamlines of stable (*S*)/unstable (*U*) steady state of flows at various Mach number. $L/D = 2$: $Re_\theta = 56.8$; $L/D = 6$: $Re_\theta = 19$. Contours represent vorticity $\omega_z D/u_\infty \in [-2, 2]$.

As we discuss in the next section, we find that the use of the stable/unstable steady states shown in figure 11 as the base states in the biglobal stability analysis yields excellent agreement in the oscillatory features in most of the cases except for a very limited number of cases where the wake mode dominates the flow. For the wake-mode dominated flow (at $Re_\theta = 19$), the mean flow can also be considered for its use as the base flow, as discussed in our companion work (Sun *et al.* 2016*a*).

Using the stable and unstable steady states, we perform extensive 2-D and 3-D linear global stability analysis. The 2-D and 3-D results are provided below in §§ 4.1 and 4.2, respectively.

4. Biglobal stability analysis

4.1. *Two-dimensional eigenmodes* ($\beta = 0$)

In the biglobal stability analysis, 2-D global eigenmodes can be found by specifying $\beta = 0$ in (2.6) and (2.7), which theoretically translates to the perturbation being associated with infinite wavelength in the spanwise direction. In this section, the stability properties are found for the base states. The eigenvalues $\omega = \omega_r + \mathrm{i}\omega_i$ obtained are reported in the non-dimensional form of the growth/decay rate $\omega_i D/u_\infty$ and frequency $St_L = \omega_r L/2\pi u_\infty$ for 2-D eigenmodes while $St_D = \omega_r D/2\pi u_\infty$ for spanwise-periodic 3-D eigenmodes.

The leading eigenmodes are shear-layer modes whose spatial structures are mainly located in the shear-layer region. Realizing that not all shear-layer modes can be called Rossiter modes, we further check that the frequencies of these shear-layer modes match the Rossiter mode frequencies predicted by the semi-empirical formula. Hence, all the leading eigenmodes herein are associated with Rossiter modes and correspond to shear-layer modes (i.e. Kelvin–Helmholtz instabilities) reported in the works by Yamouni *et al.* (2013) and Meseguer-Garrido *et al.* (2014) . The eigenvalues of Rossiter modes are listed in table 4 and their eigenvectors are shown in figures 12 and 13 for $L/D = 2$ and 6, respectively. As predicted by the semi-empirical formula, an increase in Mach number reduces the flow oscillation frequency. The spatial structure size of Rossiter modes becomes larger as Mach number increases. The spatial structures of higher-order modes exhibits finer spatial scales than those of lower-order modes. The major spatial structures of the velocity eigenmodes $\hat{u}_r$ have

https://doi.org/10.1017/jfm.2017.416 Published online by Cambridge University Press

$L/D = 2$

M_∞	I	II
0.3	$0.534 - 0.008\mathrm{i}$	$0.795 - 0.016\mathrm{i}$
0.6	$0.426 + 0.055\mathrm{i}$	$0.726 + 0.024\mathrm{i}$
0.9	$0.377 + 0.019\mathrm{i}$	$0.687 + 0.071\mathrm{i}$
1.2	$0.336 - 0.012\mathrm{i}$	$0.613 + 0.068\mathrm{i}$
1.4	$0.310 - 0.029\mathrm{i}$	$0.566 + 0.037\mathrm{i}$

$L/D = 6$

M_∞	I	II	III	IV
0.3	$0.432 - 0.057\mathrm{i}$	$0.878 + 0.092\mathrm{i}$	$1.410 + 0.027\mathrm{i}$	$1.815 - 0.042\mathrm{i}$
0.6	$0.381 - 0.000\mathrm{i}$	$0.784 + 0.081\mathrm{i}$	$1.175 + 0.069\mathrm{i}$	$1.574 - 0.005\mathrm{i}$
0.9	$0.320 - 0.006\mathrm{i}$	$0.708 + 0.030\mathrm{i}$	$1.085 + 0.020\mathrm{i}$	$1.474 - 0.028\mathrm{i}$
1.2	$0.282 - 0.032\mathrm{i}$	$0.638 - 0.008\mathrm{i}$	$0.994 - 0.014\mathrm{i}$	$1.344 - 0.046\mathrm{i}$
1.4	$0.260 - 0.048\mathrm{i}$	$0.599 - 0.035\mathrm{i}$	$0.947 - 0.045\mathrm{i}$	$1.293 - 0.088\mathrm{i}$

TABLE 4. Eigenvalues $\omega = \omega_r + \mathrm{i}\omega_i$ associated with Rossiter mode I to IV for $\beta = 0$ are reported in a form of $St_D(L/D) + \mathrm{i}(\omega_i D/u_\infty)$ at $Re_\theta = 56.8$. Frequency ω_r is normalized as Strouhal number $St_L = \omega_r L/2\pi u_\infty$ and growth/decay rate ω_i is normalized as $\omega_i D/u_\infty$.

the largest magnitude in the shear layer, which indicates that Rossiter modes are driven by the shear layer of the flow. In the pressure eigenvector contours, there are beam-shaped structures that develop above the cavity. The geometric features of these beams parallel the compression waves previously discussed in figure 5. Based on the results from both 2-D nonlinear simulations and biglobal stability analysis with $\beta = 0$, it indicates that Rossiter modes are indeed two-dimensional, shear-layer driven instabilities.

From the discussion in § 3.3 (and figures 9 and 10), the flow instability and dominant Rossiter mode shift with free stream Mach number. In the biglobal stability analysis, the growth/decay rate $\omega_i D/u_\infty$ over M_∞ is presented in figure 14. For cavity with $L/D = 2$, the growth/decay rates of Rossiter modes I and II increase as Mach number changes from 0.3 to 0.6. However, when M_∞ reaches the transonic regime, the values of growth rate show a decreasing trend. The growth rate for Rossiter mode I peaks around $M_\infty = 0.6$ and is surpassed by the growth rate of Rossiter mode II around $M_\infty = 0.7$, which reaches its peak near $M_\infty = 1$. This cross-over point corresponds to the shift from Rossiter mode I to mode II seen in figure 9(*b*). This peaking trends of growth/decay rates of Rossiter modes are also observed for the flows over cavity with $L/D = 6$. The growth rate of the eigenmode negatively correlating to the increase in free stream Mach number ($M_\infty > 0.6$) can be related to the behaviour of the neutral stability curve in the nonlinear stability diagrams shown in figure 8. Both stability diagrams indicate that an increase of Mach number in the subsonic regime ($M_\infty < 0.6$) destabilizes the flow, but over the transonic regime, an increase of Mach number ($M_\infty > 0.6$) stabilizes the flow. Furthermore, in the cases of $L/D = 2$ and $M_\infty = 0.3$, as shown in figure 14, the values of $\omega_i D/u_\infty$ are both negative. In other words, disturbances related to Rossiter modes I and II decay in the base flow, which matches the result from the stability diagram in figure 8 that the flow is stable. This agreement is also noticed in the cases of cavity with $L/D = 6$ at $M_\infty = 1.2$ and 1.4.

From the growth/decay rate trend shown in figure 14, we compare the Rossiter mode with the largest growth/decay rate at each Mach number to the dominant

https://doi.org/10.1017/jfm.2017.416 Published online by Cambridge University Press

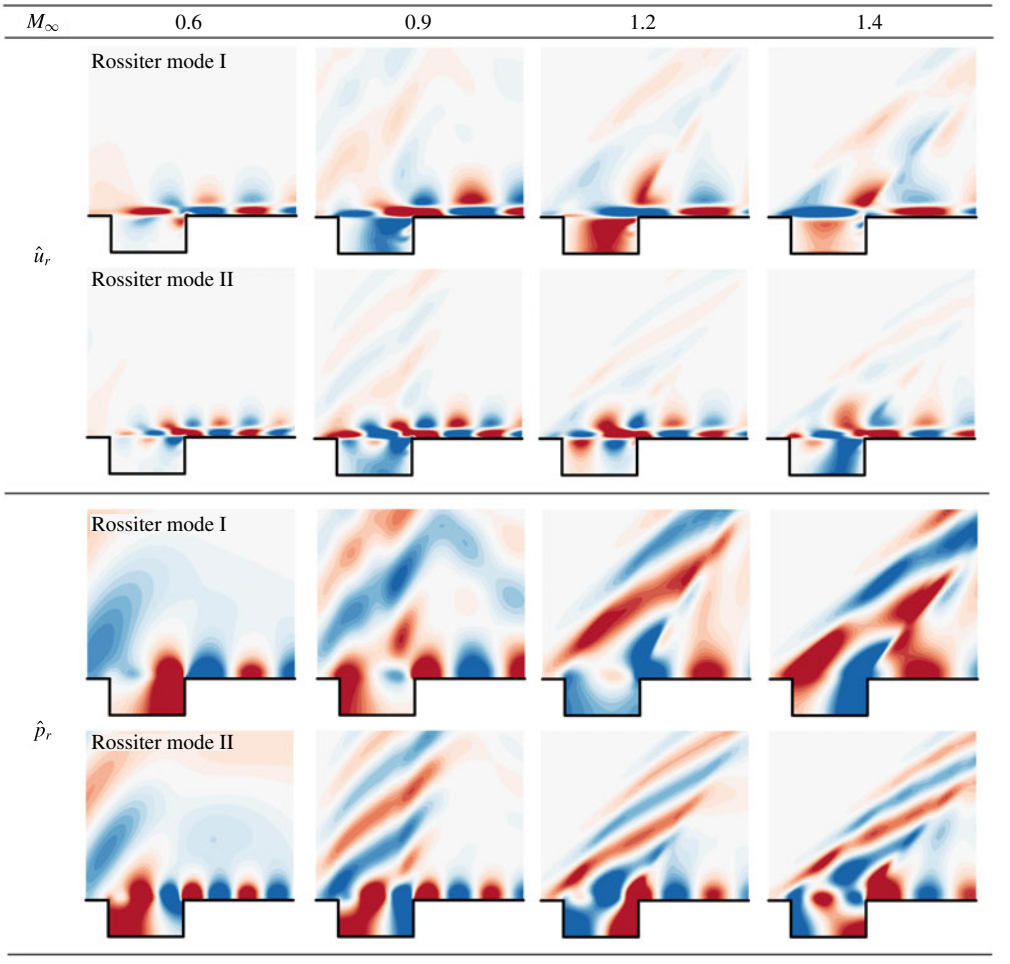


FIGURE 12. (Colour online) Spatial structures of the real component of the eigenmodes $\hat{u}$ and $\hat{p}$ for cavity of $L/D = 2$ at $Re_\theta = 56.8$.

Rossiter mode observed from the 2-D nonlinear simulations, which can explain the mode shifting presented in figures 9 and 10. In figure 15, the dominant Rossiter mode captured from linear stability analysis and nonlinear DNS discussed in § 3 are compared. In almost all cases, there is excellent agreement in the dominant Rossiter mode with respect to Mach number. At $M_\infty = 0.6$ and $L/D = 6$, the dominant Rossiter mode from biglobal stability analysis deviates from that in the DNS in which the wake mode is dominant. Moreover, the eigenvector shown in figure 13 at $M_\infty = 0.6$ resembles more closely the Rossiter modes instead of the wake mode revealed from the 2-D DNS. For this particular case, we further investigate the wake mode in our companion paper (Sun *et al.* 2016*a*). By the observation that the mean (time-averaged) flow and unstable steady state are significantly different in this wake-mode dominated flow, biglobal stability analysis was performed using both states (mean flow and unstable steady state) as base states. When the mean flow is prescribed as the base state, the wake-mode eigenmode is captured by the linear stability analysis, which can also predict its frequency with only 4 % difference between that and the wake-mode

https://doi.org/10.1017/jfm.2017.416 Published online by Cambridge University Press

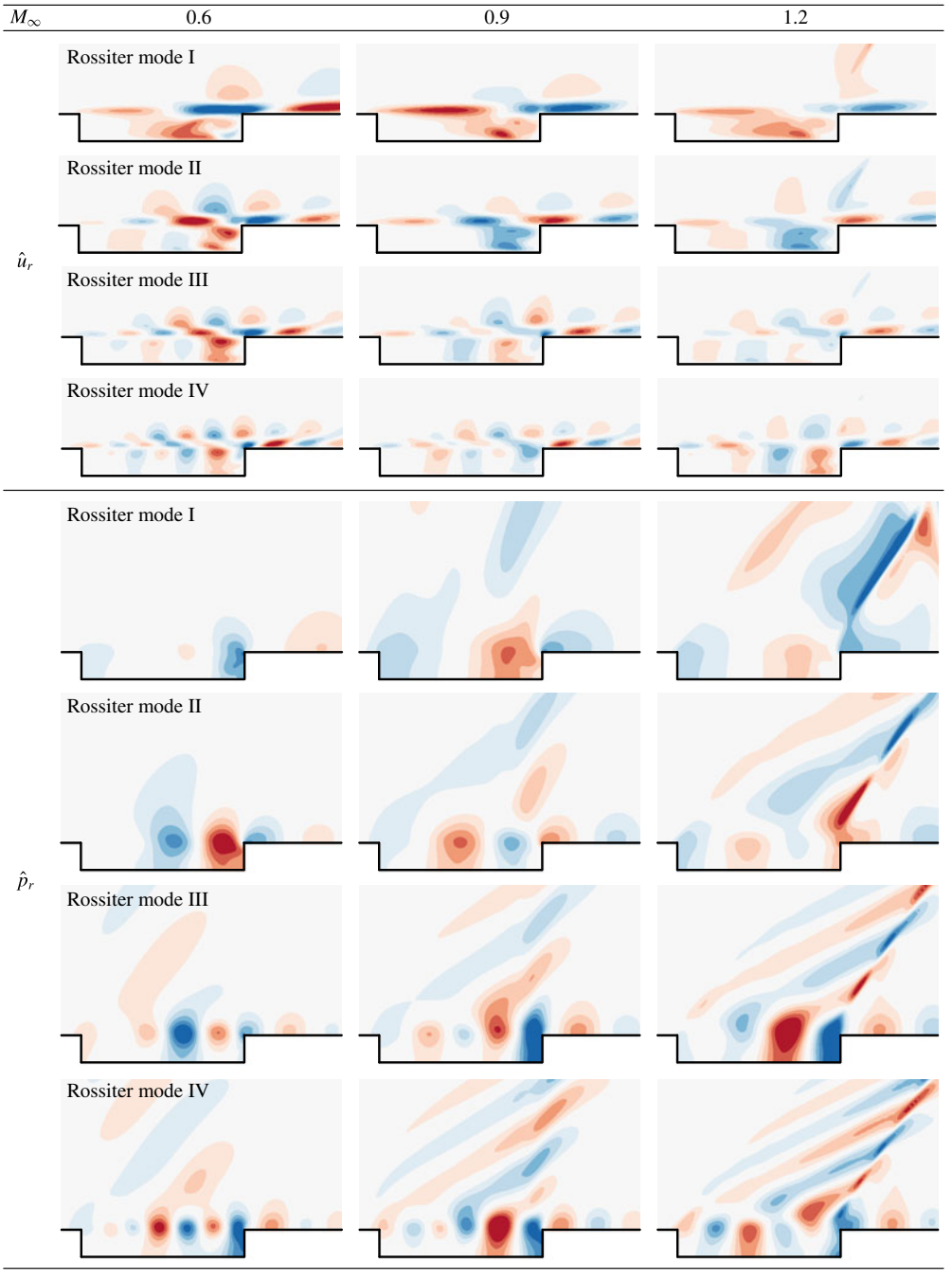


FIGURE 13. (Colour online) Spatial structures of the real component of the eigenmodes $\hat{u}$ and $\hat{p}$ for cavity of $L/D = 6$ at $Re_\theta = 19$.

frequency determined from the 2-D DNS. It should be mentioned that in the linear stability theory, the nonlinear interactions among modes are neglected. There is however a strong nonlinear dynamical process in the wake-mode dominated flow,

https://doi.org/10.1017/jfm.2017.416 Published online by Cambridge University Press

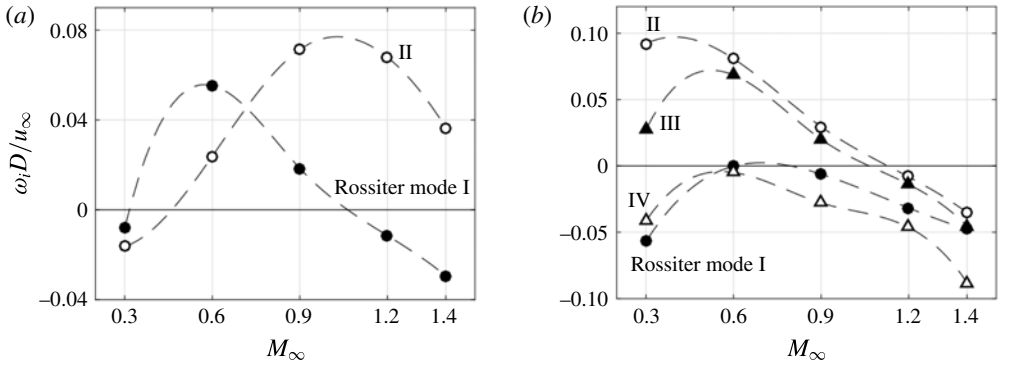


FIGURE 14. Growth/decay rates of Rossiter modes as a function of free stream Mach number determined from biglobal stability analysis with $\beta = 0$. (*a*) $L/D = 2$, $Re_\theta = 56.8$; (*b*) $L/D = 6$, $Re_\theta = 19$. Rossiter mode I: •; mode II: ○; mode III: ▲ and mode IV: △.

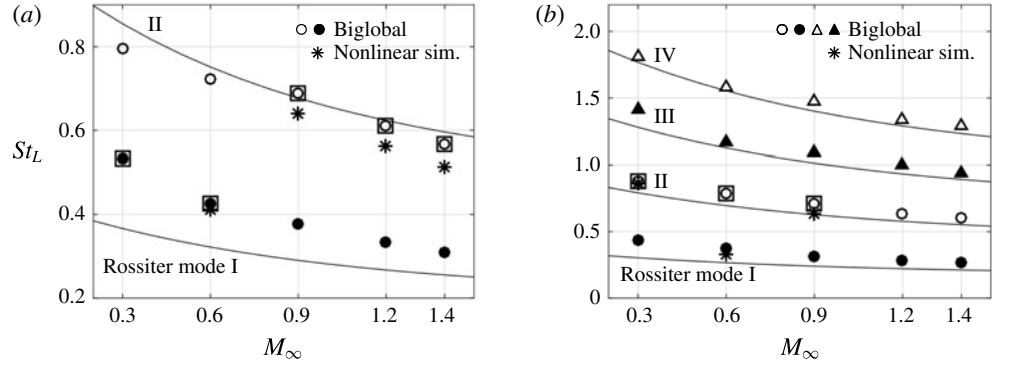


FIGURE 15. Dominant Rossiter modes captured from the 2-D nonlinear simulations and the biglobal stability analysis. (*a*) $L/D = 2$, $Re_\theta = 56.8$; (*b*) $L/D = 6$, $Re_\theta = 19$. Rossiter mode I: •; mode II: ○; mode III: ▲ and mode IV: △. The dominant Rossiter modes from the biglobal stability analysis and the nonlinear simulations are indicated by □ and ✳, respectively.

making the mean greatly deviate from the unstable steady state. Hence, the use of the mean flow as the base flow is necessary for uncovering the wake mode.

4.2. *Three-dimensional eigenmodes* ($\beta \neq 0$)

In this section, we discuss characteristics of the 3-D global instability modes with finite wavelength $\lambda/D = 2\pi/\beta$ in the spanwise direction prescribed in (2.6). The analyses performed for the 3-D instabilities are analogous to those for the 2-D cases shown in the previous section. In what follows, the spanwise wavelength λ/D is set in a range of 0.5–2.0 following Brès & Colonius (2008). Note that the 3-D instabilities discussed in this section represent spanwise-periodic 3-D instabilities with selected wavenumbers β.

The eigenspectra of the 3-D eigenmodes for $L/D = 2$ and 6 are presented in figure 16. It should be noted that the eigenspectra are only shown in the vicinity of the origin. For the $L/D = 2$ cavity flows at $Re_\theta = 56.8$, unstable 3-D modes are only

https://doi.org/10.1017/jfm.2017.416 Published online by Cambridge University Press

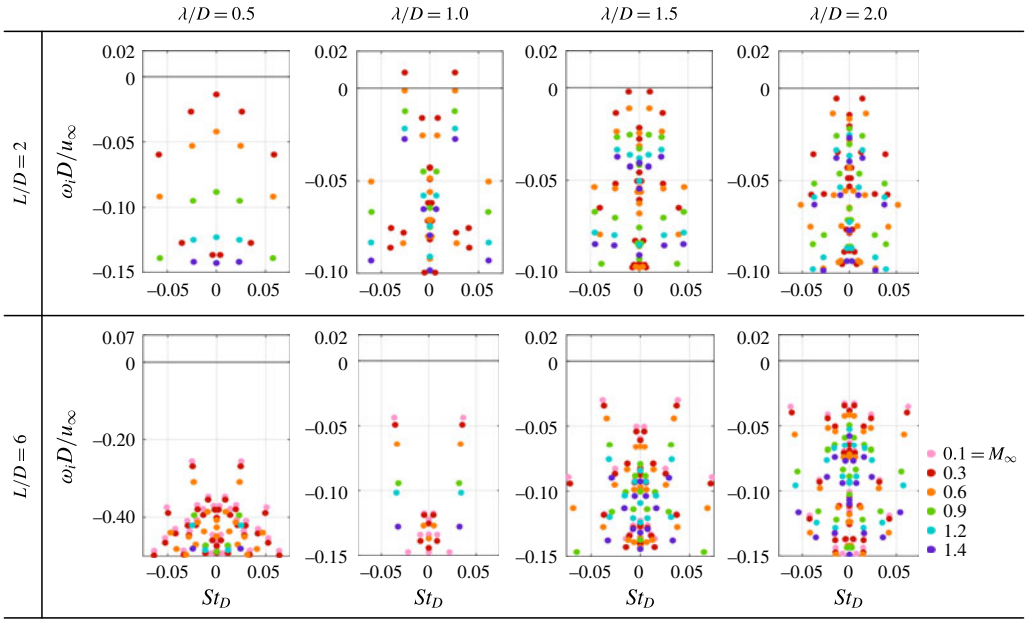


FIGURE 16. (Colour online) Eigenspectra of the 3-D eigenmodes for cavity with $L/D = 2$ ($Re_\theta = 56.8$) and 6 ($Re_\theta = 19$) with $M_\infty \in [0.1, 1.4]$ and $\lambda/D \in [0.5, 2.0]$.

observed in the subsonic cases of $M_\infty = 0.3$ with $\lambda/D = 1.0$, while all other 3-D eigenmodes with higher Mach number ($M_\infty \geqslant 0.6$) are stable. For $L/D = 6$ cases at $Re_\theta = 19$, all the 3-D eigenmodes captured are stable. Below, the effects of cavity geometry, Mach number and spanwise wavelength λ/D on the most unstable/least stable (dominant) 3-D modes are further examined.

Based on eigenspectra shown in figure 16, the eigenvalue of the most unstable/least stable eigenmode for each Mach number is extracted and plotted as a function of spanwise wavelength λ/D in figures 17 and 18. For both cavity geometries, the overall trends of growth/decay rates are similar regardless of M_∞. An increase in Mach number stabilizes all the dominant 3-D eigenmodes. For each Mach number, the growth/decay rate $\omega_i D/u_\infty$ of the dominant 3-D eigenmode is a function of λ/D. To identify the 3-D eigenmode properties, their frequencies and spatial structures can distinguish the modes based on types of instabilities.

We follow the nomenclature used by Brès & Colonius (2008) for the leading modes in figures 17 and 18. As shown in figure 17 for cavity with $L/D = 2$, the leading eigenmode with $\lambda/D = 0.5$ is mode i with $St_D = 0$ (referred to as mode i by Brès & Colonius (2008)) except at $M_\infty = 1.4$. The dominant 3-D mode at $M_\infty = 1.4$ is mode ii, a travelling mode discussed next. However, its decay rate is close to that of a stationary mode as shown in figure 16. The eigenmodes with $\lambda/D \in [0.75, 1.25]$ are travelling modes with $St_D \approx 0.025$ (referred to as mode ii by Brès & Colonius (2008)). For each of $\lambda/D \leqslant 1.25$, the frequency, St_D, of all the dominant 3-D modes are independent of Mach number, but these 3-D modes can be stabilized by increasing M_∞ as mentioned above. However, the frequencies of the dominant 3-D modes exhibit a sudden decrease near $\lambda/D = 1.5$, and the modes exhibit different branches for larger λ/D ($\geqslant 1.75$) depending on Mach numbers. As shown in figure 17, for the flows at $0.3 \leqslant M_\infty \leqslant 0.6$, the dominant modes are travelling modes with $St_D \approx 0.015$ (referred

https://doi.org/10.1017/jfm.2017.416 Published online by Cambridge University Press

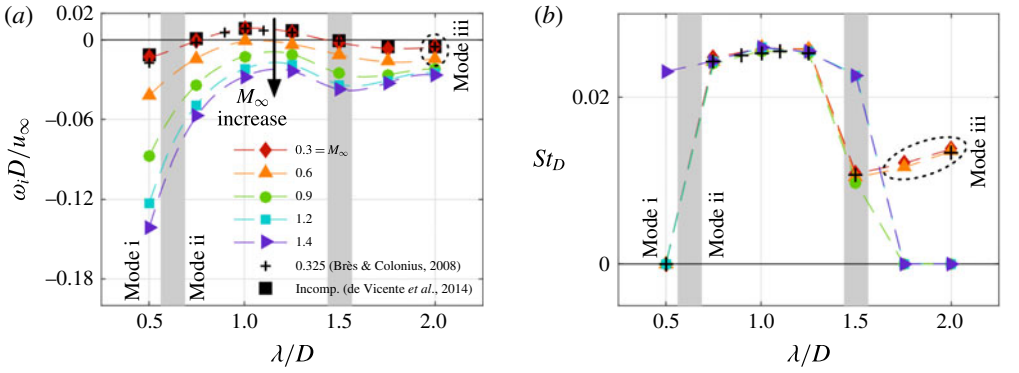


FIGURE 17. (Colour online) Eigenvalues of the dominant 3-D modes as a function of M_∞ and spanwise wavelength λ/D for cavity with $L/D = 2$ at $Re_\theta = 56.8$. (*a*) Growth/decay rate $\omega_i D/u_\infty$; (*b*) frequency St_D. Results from Brès & Colonius (2008) and de Vicente *et al.* (2014) are also compared to the present results. The grey regions represent the transitions of dominant modes.

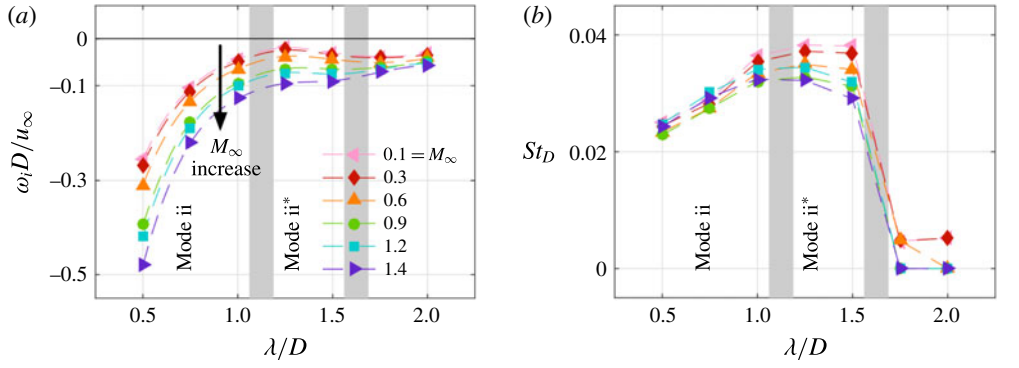


FIGURE 18. (Colour online) Eigenvalues of the dominant 3-D modes as a function of M_∞ and spanwise wavelength λ/D for cavity with $L/D = 6$ at $Re_\theta = 19$. (*a*) Growth/decay rate $\omega_i D/u_\infty$; (*b*) frequency St_D. The grey regions represent the transitions of dominant modes.

to as mode iii by Brès & Colonius (2008)), while for the transonic flows at $0.9 \leqslant M_\infty \leqslant 1.4$, the dominant modes are stationary. Moreover, we indicate the transitions of dominant modes over the spanwise wavelength in figure 17 by grey regions. As the wavelength of the 3-D eigenmode is increased from 0.5 to 2, in general, the dominant 3-D mode shifts from stationary to travelling mode and back to stationary mode. This phenomenon was also reported by de Vicente *et al.* (2014) on incompressible cavity flows that the dominant 3-D mode can arise from different instabilities in terms of its spanwise wavelength.

For the eigenvalues in the case of a cavity with $L/D = 6$ presented in figure 18, the dominant 3-D mode with $\lambda/D = 0.5$ is the travelling mode or mode ii ($St_D \approx 0.025$) as mentioned above for the case of short cavity. We further note that the dominant mode has characteristics of mode ii type, as we later discuss in the spatial structures of the eigenmodes (in figure 19). The dominant 3-D modes with $\lambda/D = 0.75$ and 1.0 have higher frequencies compared to that of smaller wavelengths, but their eigenvectors still share similarities, as shown later. There is another mode having

https://doi.org/10.1017/jfm.2017.416 Published online by Cambridge University Press

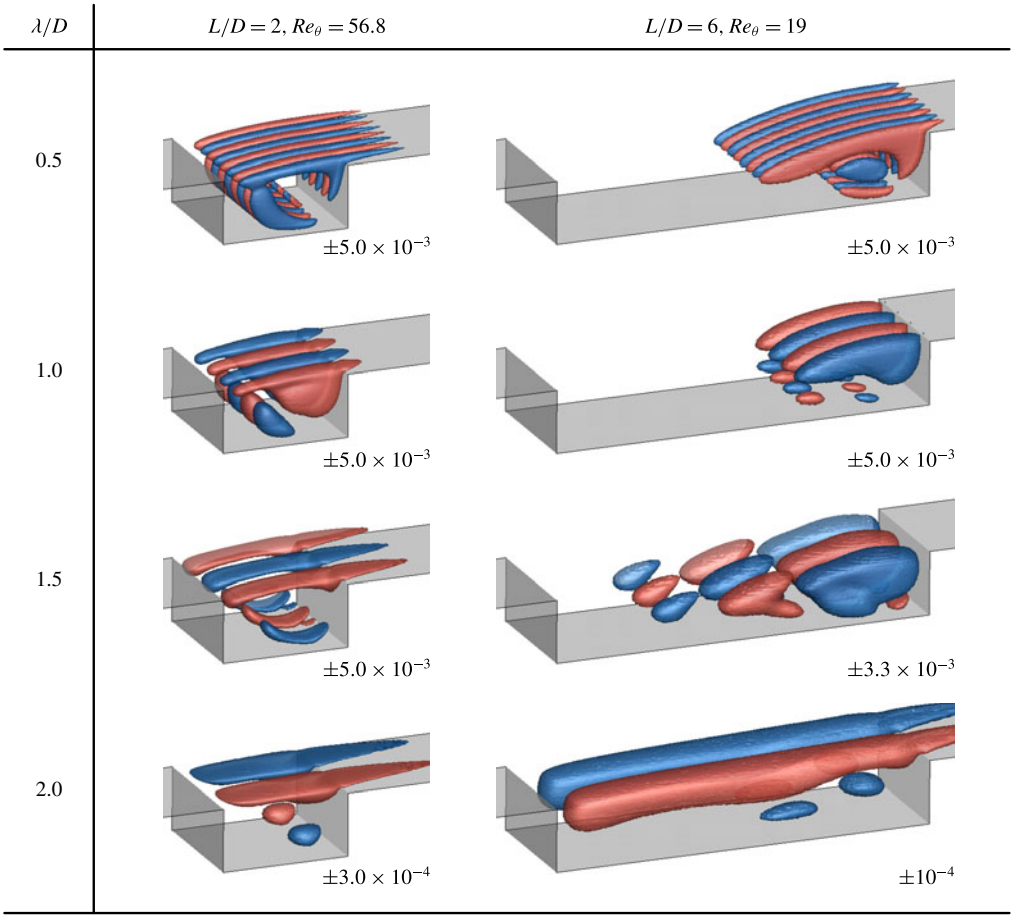


FIGURE 19. (Colour online) Iso-surface of eigenvectors of the least stable 3-D eigenmodes at $M_\infty = 0.9$ and spanwise wavelength $\lambda/D \in [0.5, 2.0]$. The values selected to show the iso-surface of $\hat{u}_r/u_\infty$ are indicated below each panel. Red and blue colours represent the indicated positive and negative values, respectively.

frequency $St_D \in [0.03, 0.04]$ with $\lambda/D = 1.25$ and 1.5, which is denoted as mode ii* due to the variation in both frequency and eigenvector compared to mode ii. As λ/D increases from 1.5 to 1.75, the dominant mode changes from a travelling mode to a stationary mode. With $\lambda/D = 1.75$ and 2.0, there is similarity to the cases of short cavity, in which the dominant 3-D modes are nearly stationary. For the subsonic flows with $0.1 \leqslant M_\infty \leqslant 0.6$, these 3-D modes possess non-zero frequencies, but with relatively small St_D compared to the other travelling modes. A decreasing trend in the growth/decay rates at $\lambda/D = 1.5$ is observed as shown in figure 18, which is similar to those captured for the short cavity. However, the possible mode transitions in the region of $0.5 \leqslant \lambda/D \leqslant 1.5$ is not distinctly clear based on the properties of the eigenvalues, which is further discussed below.

The spatial structures of the dominant 3-D eigenmodes are illustrated in figure 19 for different values of λ/D. For the short cavity with $L/D = 2$, the eigenvectors obtained for all Mach numbers considered are similar in terms of the spatial structures. For all values of λ/D considered, the eigenvectors show variations in

https://doi.org/10.1017/jfm.2017.416 Published online by Cambridge University Press

the aft part of the cavity where the major recirculation zone is located as shown in the unstable steady states shown in figure 11, while their structures are also present in the shear-layer region of the flows. Brès & Colonius (2008) examined the 3-D instabilities as well at $M_\infty = 0.3$ and argued that these 3-D modes result from the centrifugal instability of the recirculation in the base flows.

For the cavity with $L/D = 6$, the spatial structures of the dominant 3-D eigenmodes also appear independent of the Mach number, as in the case of $L/D = 2$. As shown in figure 19, in the cases of $\lambda/D = 0.5$ and 1.0, the spatial structures of mode ii are located in the rear part of the cavity, which exhibit similar features to those presented in the shorter cavity, but with the eigenmodes extending upstream along the shear layer. The spatial structures of mode ii* ($\lambda/D = 1.5$) align along the floor from the rear towards the mid-region of the cavity, which is significantly different from the mode ii that stems from centrifugal instabilities. The streamwise-stretched recirculation pattern in the unstable steady state shown in figure 11 appears due to the large aspect ratio of the long cavity. This elongated recirculating flow is likely the reason for the formation of the mode ii*, which explains the absence of mode ii* in the short cavity flows. For the stationary mode for $\lambda/D = 2.0$, its spatial structure covers the entire length of the cavity. Although the frequency of the 3-D mode with $\lambda/D = 2.0$ in the subsonic regime ($M_\infty = 0.1 - 0.6$) is not exactly zero, the eigenvectors still share similar features to the stationary mode. The spatial structures of 3-D instability modes appear to be strongly influenced by their spanwise wavelengths in the long cavity cases, and the leading eigenmode can be a travelling or stationary mode depending on λ/D.

In the work by Liu *et al.* (2016) that side wall effects are considered with triglobal stability analysis for incompressible cavity flow with $L/D = 6$, they concluded that shear-layer instability is dominant in finite-span cavity flow. This is also observed in the present study on spanwise homogeneous cavity flow at $M_\infty = 0.3$ that the most unstable mode is found to be the shear-layer mode (Rossiter mode), while centrifugal instability modes are stable. The major difference appears in the spatial structure of shear-layer mode due to cavity geometries; a narrow finite-span cavity in their work and a spanwise homogeneous cavity in the present work.

4.3. *Comparison with DNS*

Next, let us compare our findings from linear stability analysis with those from DNS. Three-dimensional DNS with $W/D = 2$ are performed at $M_\infty = 0.6$ for both short and long cavities. For the cavity with $L/D = 2$ ($Re_\theta = 56.8$), Fourier spectra of velocity are shown in figure 20. The comparison of dominant frequencies, St_D, obtained from DNS and biglobal stability analysis are listed in table 5. In the 3-D DNS of $L/D = 2$, the dominant 2-D mode is Rossiter mode II. However, in 2-D DNS and biglobal stability analysis with $\lambda/D = \infty$, the Rossiter mode I is the dominant mode. By performing the simulation over a sufficiently long time, the travelling mode with $St_D = 0.027$ at $\lambda/D = 1.0$ is observed in the 3-D DNS. Its properties have excellent agreement to those of the leading 3-D mode shown in figure 17, in which mode ii with $\lambda/D = 1.0$ has the largest $\omega_i D/u_\infty = -0.0013$ among all the λ/D considered. Although this mode has negative growth rate, in the 3-D nonlinear simulation, unstable 2-D Rossiter mode and 3-D modes could interact via nonlinearities and result in the existence of the 3-D mode in the nonlinear flows, especially when the eigenvalue is close to the neutral stability line ($\omega_i D/u_\infty = 0$). The comparison of the 3-D spatial structures of nonlinear flow and travelling mode ii are displayed in figure 21, where instantaneous

https://doi.org/10.1017/jfm.2017.416 Published online by Cambridge University Press

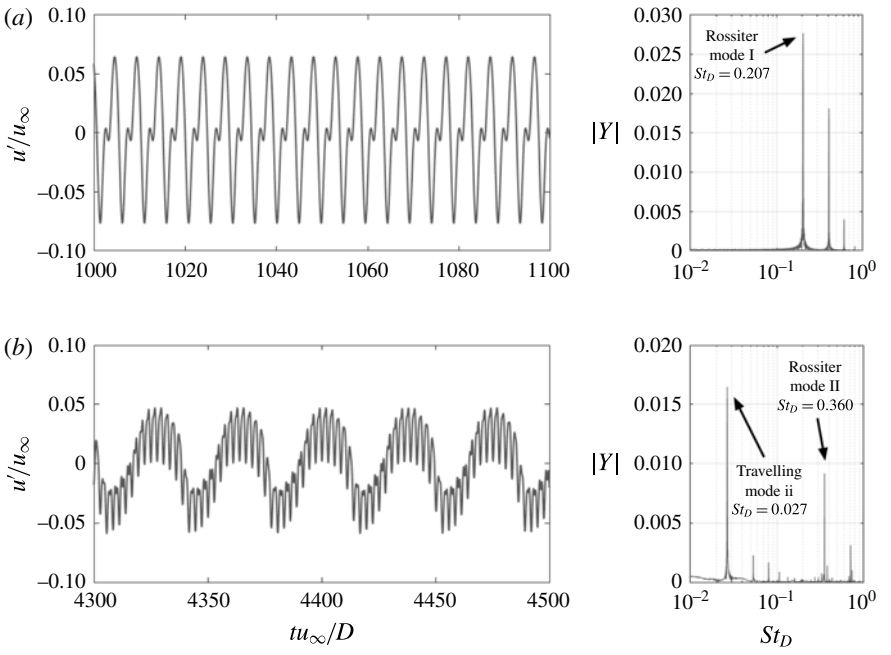


FIGURE 20. Time histories of streamwise velocity perturbation u'/u_∞ collected by a probe located at $x/D = 1$, $y/D = 0$, $z/D = 1$ are shown on the left. The corresponding Fourier spectra are presented on the right. (*a*) 2-D DNS and (*b*) 3-D DNS ($W/D = 2$) for $L/D = 2$, $Re_\theta = 56.8$ and $M_\infty = 0.6$.

flow fields and eigenmode with a quarter period interval are presented. Mode ii shown in figure 21 has qualitatively similar spatial structures to the eigenfunction of Mode I found by Meseguer-Garrido *et al.* (2014) at a similar incompressible flow condition. In their work, this mode is unstable in incompressible conditions. In contrast, mode ii is slightly stable in the present work at $M_\infty = 0.6$, which agrees with the discussion in § 4.3 that an increase in Mach number can stabilize 3-D eigenmodes. The iso-surface of spanwise velocity w/u_∞ from nonlinear simulation exhibits comparable structures to those of mode ii. In particular, the 2-D Rossiter mode also appears in the nonlinear DNS, in which streamwise distortions of the spatial structures are observable in the shear-layer region.

For the cavity with $L/D = 6$ ($Re_\theta = 19$), the violent wake mode present in 2-D DNS is not observed in 3-D DNS. Instead, Rossiter mode II dominates the flow. When the flow has reached steady oscillations, there is no evident low-frequency peaks of the 3-D structures in the nonlinear flows. In the comparison of the 3-D spatial structures revealed by the 3-D DNS and 3-D eigenmodes as shown in figure 22, we find that for the 3-D nonlinear flows, the spatial structures located in the rear region of the cavity stay almost stationary in the spanwise direction with wavelength of $\lambda/D = 2$, while those obtained from the linear stability analysis are distributed in the front and rear regions of the cavity. As shown in figure 18, though all the 3-D eigenmodes have negative values of growth rate, the spatial structures of 2-D Rossiter modes (figure 13) and 3-D eigenmodes (figure 19) overlap in the rear part of the cavity, which can lead to modal interactions and modify the instabilities predicted from biglobal stability analysis.

https://doi.org/10.1017/jfm.2017.416 Published online by Cambridge University Press

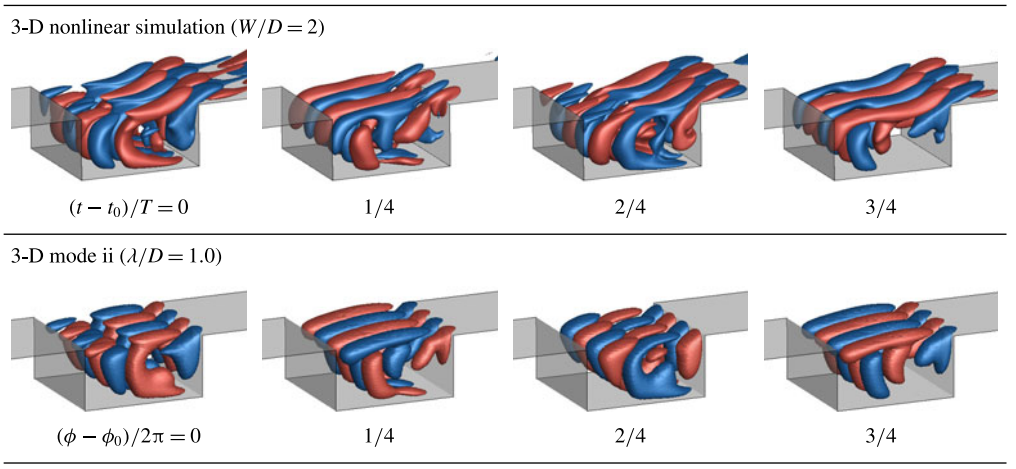


FIGURE 21. (Colour online) Comparison of the iso-surface of the spanwise velocity $w/u_\infty = \pm 0.013$ from the 3-D nonlinear simulation and $\hat{w}/u_\infty = \pm 0.03$ from the dominant 3-D eigenmode with $\lambda/D = 1.0$ for the cavity with $L/D = 2$ at $M_\infty = 0.6$ and $Re_\theta = 56.8$. Represented by T is the time period of the 3-D mode captured by the nonlinear simulation, t_0 and ϕ_0 are reference time and phase, respectively. Red and blue colours represent positive and negative values, respectively.

	St_D		λ/D
2-D DNS	0.207	Rossiter mode I*	∞
Biglobal stability	0.213	Rossiter mode I*	∞
	0.026	Travelling mode ii	1.0
3-D DNS	0.360	Rossiter mode II*	∞
	0.027	Travelling mode ii	1.0

TABLE 5. Comparison of the frequencies of the dominant modes obtained from DNS and biglobal stability analysis for $L/D = 2$, $Re_\theta = 56.8$ and $M_\infty = 0.6$. Dominant mode is denoted with *.

In the 3-D DNS, the large vortex roll ups of wake mode present in the 2-D DNS is no longer observable. Meanwhile, the spanwise motion becomes evident in the 3-D flows. To uncover these spanwise effects on the long cavity, further analysis has been performed in our companion work (Sun *et al.* 2016*a*), in which we found that the presence of spanwise motion (or three-dimensionalities) in the flow can preclude the formation of the wake mode, reducing the intense fluctuations of the flow. This observation suggests the potential to reduce cavity flow oscillations by introducing spanwise variations to the base flows. In order to weaken the strength of the impingement of shear layer on the trailing edge of the cavity, we can trigger the emergence of 3-D global modes and achieve energy redistribution from spanwise vortices to streamwise vortical structures. To retain the energy inside the cavity, the spanwise wavelength of perturbation introduced to the flow should be in the range of 0.5–1.5, since the spatial structures of 3-D modes associated with these wavelengths mainly stay inside the cavity, which has been illustrated in figure 19.

https://doi.org/10.1017/jfm.2017.416 Published online by Cambridge University Press

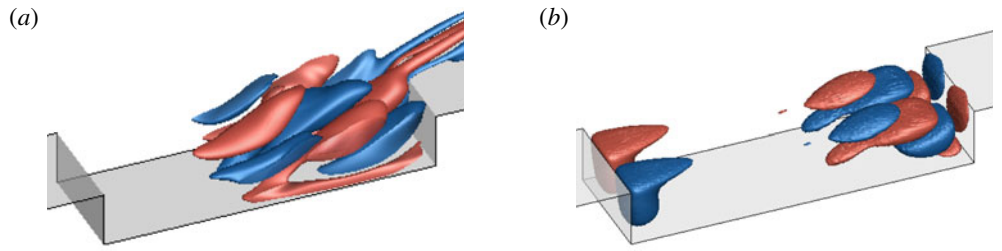


FIGURE 22. (Colour online) Comparison of the iso-surface of the instantaneous spanwise velocity $w/u_\infty = \pm 0.083$ from the 3-D nonlinear simulation and $\hat{w}/u_\infty = \pm 0.083 \times 10^{-3}$ from the dominant 3-D eigenmode (stationary mode) with $\lambda/D = 2.0$ for the cavity with $L/D = 6$ and $M_\infty = 0.6$ and $Re_\theta = 19$. Red and blue colours represent positive and negative values, respectively.

To verify this concept of using 3-D instability to reduce cavity flow oscillations, we note in passing that 3-D slot jets can be introduced along the leading edge of the cavity to alter the flow features. The performance of these control strategies via 3-D steady blowing for cavity flows is assessed by Zhang *et al.* (2015) and George *et al.* (2015) through a large number of experiments and some representative large-eddy simulations. They find that the wavelengths for effective 3-D flow control to reduce cavity flow oscillations are in good agreement with the findings of present global stability analysis. Although the idea of 3-D flow control is not new (Zdravkovich 1981), the present work particularly uncovers the temporal instabilities affected by compressibility in the transonic regime. Moreover, the spanwise wavelength and frequency associated with 3-D instabilities are identified, which can be useful in examining the influence of flow parameters for 3-D flow control designs. We believe that the insights from the global instability characteristics of compressible open-cavity flows can provide valuable information for designing physics-based flow control strategies.

5. Conclusions

Two- and three-dimensional biglobal instabilities of two-dimensional compressible open-cavity flows are examined for rectangular cavities with aspect ratios of $L/D = 2$ and 6. Noteworthy in the present work is the focus on the global instability analysis for long cavity ($L/D = 6$) flows in the transonic regime, which have not been examined in detail in the past, despite their importance in being representative of practical cavity applications on aircraft. Direct numerical simulations and biglobal stability analysis are used to uncover the influence of Mach number, Reynolds number and spanwise wavelength on the 2-D and 3-D global instability modes with respect to the 2-D steady states. In the 2-D DNS, we find that an increase in Mach number in the subsonic regime destabilizes the flow but stabilizes the flow in the transonic regime at low Reynolds number for both short ($L/D = 2$) and long ($L/D = 6$) cavities, which agrees with the findings from the work by Yamouni *et al.* (2013) on flows over short cavities ($L/D = 1$ and 2). Moreover, the dominant Rossiter mode can shift due to the variation in the free stream Mach number.

The 2-D eigenmodes obtained from biglobal stability analysis exhibit excellent agreement with the properties of the 2-D flow characteristics uncovered from 2-D

https://doi.org/10.1017/jfm.2017.416 Published online by Cambridge University Press

DNS, indicating that these 2-D global modes are Rossiter modes driven by the shear layer. Through the 2-D eigen-analysis with $\beta = 0$, destabilization and subsequent stabilization effects via increasing Mach number is captured. Moreover, a shift in the dominant Rossiter mode is observed with Mach number variation, which explains the mode shifting behaviour in 2-D nonlinear simulation results.

In contrast to the 2-D modes, the dominant 3-D modes unravelled in the present work are instabilities that are largely unaffected by a change in Mach number. Although an increase in Mach number stabilizes all 3-D eigenmodes, the overall behaviour of 3-D eigenmodes as a function of the spanwise wavelength λ/D is almost independent of the Mach number. However, the type of dominant 3-D mode is strongly dependent on λ/D. For the short cavity with $L/D = 2$, the most unstable/least stable 3-D modes have $\lambda/D \in [1.0, 1.25]$ (mode ii) stemming from centrifugal instabilities for almost all Mach numbers considered, as reported by Brès & Colonius (2008). For the long cavity with $L/D = 6$, the least stable 3-D modes have $\lambda/D = 1.25$ and 2.0 for cases of $M_\infty \lesssim 0.3$ and $M_\infty \gtrsim 0.6$, respectively. Moreover, there are additional types of eigenmodes for this long cavity flow possessing various spatial structures compared to those of the shorter cavity.

In 3-D DNS, both frequencies and spatial structures of the leading 3-D mode seen in the DNS correspond closely to the results of the linear biglobal stability analysis of the dominant 3-D eigenmode for $L/D = 2$. However, for $L/D = 6$, 3-D DNS reveals large roll up of the cavity shear layer, which indicates strong nonlinearities that depart from the linear analysis. Nevertheless, the insights from global stability analysis provide a potential pathway to reduce flow oscillations by introducing spanwise variations to the base flows, which has been demonstrated in the experiments by Lusk *et al.* (2012), George *et al.* (2015) and Zhang *et al.* (2015). The analyses in this study provide valuable knowledge on global instabilities of 2-D and 3-D compressible open-cavity flows, which can be leveraged in designing physics-based flow control strategies in upcoming studies.

Acknowledgements

This work was supported by the U.S. Air Force Office of Scientific Research (Grant no.: FA9550-13-1-0091, Program Managers: Drs D. Smith and I. Leyva). The high performance computing resource was provided by the Research Computing Center at the Florida State University. The authors also acknowledge the insightful discussions with Dr G. A. Brès.

REFERENCES

AHUJA, K. K. & MENDOZA, J. 1995 Effects of cavity dimensions, boundary layer and temperature on cavity noise with emphasis on benchmark data to validate computational aeroacoustic codes. *Final Report Contract* NAS1-19061, Task 13. NASA Contractor Report.

ÅKERVIK, E., BRANDT, L., HENNINGSON, D. S., HŒPFFNER, J., MARXEN, O. & SCHLATTER, P. 2006 Steady solutions of the Navier–Stokes equations by selective frequency damping. *Phys. Fluids* **18**, 068-102.

ARUNAJATESAN, S., BARONE, M. F., WAGNER, J. L., CASPER, K. M. & BERESH, S. J. 2014 Joint experimental/computational inversigation into the effects of finite width on transonic cavity flow. *AIAA Paper* 2014-3027.

BERESH, S. J., WAGNER, J. L. & CASPER, K. M. 2016 Compressibility effects in the shear layer over a rectangular cavity. *J. Fluid Mech.* **808**, 116–152.

https://doi.org/10.1017/jfm.2017.416 Published online by Cambridge University Press

BERESH, S. J., WAGNER, J. L., PRUETT, B. O. M., HENFLING, J. F. & SPILLERS, R. W. 2015 Supersonic flow over a finite-width rectangular cavity. *AIAA J.* **53** (2), 296–310.

BERGAMO, L. F., GENNARO, E. M., THEOFILIS, V. & MEDEIROS, M. A. F. 2015 Compressible modes in a square lid-driven cavity. *Aerosp. Sci. Technol.* **44** (C), 125–134.

BRÈS, G. A. 2007 Numerical simulations of three-dimensional instabilities in cavity flows. PhD thesis, California Institute of Technology.

BRÈS, G. A. & COLONIUS, T. 2008 Three-dimensional instabilities in compressible flow over open cavities. *J. Fluid Mech.* **599**, 309–339.

BRÈS, G. A., HAM, F. E., NICHOLS, J. W. & LELE, S. K. 2017 Unstructured large-eddy simulations of supersonic jets. *AIAA J.* **55** (4), 1164–1184.

CATTAFESTA, L. N., GARG, S., CHOUDHARI, M. & LI, F. 1997 Active control of flow-induced cavity resonance. *AIAA Paper* 1997-1804.

CATTAFESTA, L. N. & SHEPLAK, M. 2011 Actuators for active flow control. *Annu. Rev. Fluid Mech.* **43**, 247–272.

CATTAFESTA, L. N., SONG, Q., WILLIAMS, D. R., ROWLEY, C. W. & ALVI, F. S. 2008 Active control of flow-induced cavity oscillations. *Prog. Aeronaut. Sci.* **44**, 479–502.

COLONIUS, T., BASU, A. J. & ROWLEY, C. W. 1999 Numerical investigation of the flow past a cavity. *AIAA Paper* 1999–1912.

FREUND, J. B. 1997 Proposed inflow/outflow boundary condition for direct computation of aerodynamic sound. *AIAA J.* **35** (4), 740–742.

GEORGE, B., UKEILEY, L., CATTAFESTA, L. N. & TAIRA, K. 2015 Control of three-dimensional cavity flow using leading edge slot blowing. *AIAA Paper* 2015-1059.

GHARIB, M. & ROSHKO, A. 1987 The effect of flow oscillations on cavity drag. *J. Fluid Mech.* **177**, 501–530.

HELLER, H. H. & BLISS, D. B. 1975 The physical mechanism of flow-induced pressure fluctuations in cavities and concepts for their suppression. *AIAA Paper* 1975-491.

KEGERISE, M. A., SPINA, E. F., GARG, S. & CATTTAFESTA, L. N. 2004 Mode-switching and nonlinear effects in compressible flow over a cavity. *Phys. Fluids* **16** (3), 678–686.

KHALIGHI, Y., HAM, F., MOIN, P., LELE, S., SCHLINKER, R., REBA, R. & SIMONICH, J. 2011*a* Noise prediction of pressure-mismatched jets using unstructured large eddy simulation. *Proceedings of ASME Turbo Expo, Vancouver*.

KHALIGHI, Y., NICHOLS, J. W., HAM, F., LELE, S. K. & MOIN, P. 2011*b* Unstructured large eddy simulation for prediction of noise issued from turbulent jets in various configurations. *AIAA Paper* 2011–2886.

KRISHNAMURTY, K. 1956 Sound radiation from surface cutouts in high speed flow. PhD thesis, California Institute of Technology.

LAWSON, S. J. & BARAKOS, G. N. 2011 Review of numerical simulations for high-speed, turbulent cavity flows. *Prog. Aeronaut. Sci.* **47**, 186–216.

LIU, Q., GÓMEZ, F. & THEOFILIS, V. 2016 Linear instability analysis of low-*Re* incompressible flow over a long rectangular finite-span open cavity. *J. Fluid Mech.* **799**, R2.

LUSK, T., CATTAFESTA, L. & UKEILEY, L. S. 2012 Leading-edge slot blowing on an open cavity in supersonic flow. *Exp. Fluids* **53**, 187–199.

MAULL, D. J. & EAST, L. F. 1963 Three-dimensional flow in cavities. *J. Fluid Mech.* **16**, 620–632.

MESEGUER-GARRIDO, F., DE VICENTE, J., VALERO, E. & THEOFILIS, V. 2014 On linear instability mechanisms in incompressible open cavity flow. *J. Fluid Mech.* **752**, 219–236.

ROCKWELL, D. & NAUDASCHER, E. 1978 Review-self-sustaining oscillations of flow past cavities. *Trans. ASME J. Fluids Engng* **100**, 152–165.

ROSSITER, J. E. 1964 Wind-tunnel experiments on the flow over rectangular cavities at subsonic and transonic speeds. *Tech. Rep.* 3438. Aeronautical Research Council Reports and Memoranda.

ROWLEY, C. W., COLONIUS, T. & BASU, A. J. 2002 On self-sustained oscillations in two-dimensional compressible flow over rectangular cavities. *J. Fluid Mech.* **455**, 315–346.

SAMIMY, M., KIM, J. H., KASTNER, J., ADAMOVICH, I. & UTKIN, Y. 2007 Active control of high-speed and high-Reynolds-number jets using plasma actuators. *J. Fluid Mech.* **578**, 305–330.

https://doi.org/10.1017/jfm.2017.416 Published online by Cambridge University Press

SAROHIA, V. 1975 Experimental and analytical investigation of oscillations in flows over cavities. PhD thesis, California Institute of Technology.

SORENSEN, D., LEHOUCQ, R., YANG, C. & MASCHHOFF, K. 1996–2008 ARPACK software.

SUN, Y., NAIR, A. G., TAIRA, K., CATTAFESTA, L. N., BRÈS, G. A. & UKEILEY, L. S. 2014 Numerical simulation of subsonic and transonic open-cavity flows. *AIAA Paper* 2014-3092.

SUN, Y., TAIRA, K., CATTAFESTA, L. N. & UKEILEY, L. S. 2016*a* Spanwise effects on instabilities of compressible flow over a long rectangular cavity. *Theor. Comput. Fluid Dyn.* (in press).

SUN, Y., ZHANG, Y., TAIRA, K., CATTAFESTA, L., GEORGE, B. & UKEILEY, L. 2016*b* Width and sidewall effects on high speed cavity flows. *AIAA Paper* 2016-1343.

THEOFILIS, V. 2003 Advances in global linear instability analysis of nonparallel and three-dimensional flows. *Prog. Aeronaut. Sci.* **39**, 249–315.

THEOFILIS, V. & COLONIUS, T. 2004 Three-dimensional instabilities of compressible flow over open cavities: direct solution of the biglobal eigenvalue problem. *AIAA Paper* 2004-2544.

TORO, E. F. 2009 *Riemann Solvers and Numerical Methods for Fluid Dynamics*. Springer.

DE VICENTE, J., BASLEY, J., MESEGUER-GARRIDO, F., SORIA, J. & THEOFILIS, V. 2014 Three-dimensional instabilities over a rectangular open cavity: from linear stability analysis to experimentation. *J. Fluid Mech.* **748**, 189–220.

WHITE, F. 1991 *Viscous Fluid Flow*. McGraw-Hill.

YAMOUNI, S., SIPP, D. & JACQUIN, L. 2013 Interaction between feedback aeroacoustic and acoustic resonance mechanisms in a cavity flow: a global stability analysis. *J. Fluid Mech.* **717**, 134–165.

ZDRAVKOVICH, M. M. 1981 Review and classification of various aerodynamic and hydrodynamic means for suppressing vortex shedding. *J. Wind Engng Ind. Aerodyn.* **7** (2), 145–189.

ZHANG, K. & NAGUIB, A. M. 2011 Effect of finite cavity width on flow oscillation in a low-Mach-number cavity flow. *Exp. Fluids* **51** (5), 1209–1229.

ZHANG, Y., SUN, Y., ARORA, N., CATTAFESTA, L., TAIRA, K. & UKEILEY, L. 2015 Suppression of cavity oscillations via three-dimensional steady blowing. *AIAA Paper* 2015-3219.

https://doi.org/10.1017/jfm.2017.416 Published online by Cambridge University Press